Ore Geology Reviews 162 (2023) 105667

Contents lists available at ScienceDirect

Ore Geology Reviews

journal homepage: www.elsevier.com/locate/oregeorev

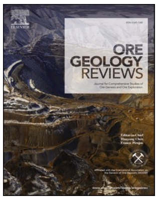

New insights on the formation of the Jingchong Cu-Co-Pb-Zn deposit, South China: Evidence from sphalerite mineralogy and muscovite ^{40}Ar-^{39}Ar dating

Erke Peng [a,b], Jochen Kolb [b,c], Benjamin F. Walter [b,c], Max Frenzel [d], Clifford G.C. Patten [b,c], Deru Xu [e], Yufei Wang [a], Jing Gan [a], Aratz Beranoaguirre [b,c], Zhilin Wang [a,*]

[a] *Key Laboratory of Metallogenic Prediction of Nonferrous Metals and Geological Environment Monitoring, Ministry of Education, School of Geosciences and Info-Physics, Central South University, Changsha 410083, China*
[b] *Karlsruhe Institute of Technology (KIT), Chair of Economic Geology and Geochemistry, Adenauerring 20b, 76131 Karlsruhe, Germany*
[c] *Laboratory for Environmental and Raw Materials Analyses (LERA), Adenauerring 20b, 76131 Karlsruhe, Germany*
[d] *Helmholtz-Zentrum Dresden-Rossendorf, Institute Freiberg for Resource Technology, Chemnitzer Str. 40, 09599 Freiberg, Germany*
[e] *State Key Laboratory of Nuclear Resources and Environment, East China University of Technology, Nanchang 330013, China*

ARTICLE INFO

Keywords:
Sphalerite
^{40}Ar-^{39}Ar dating
Jingchong polymetallic deposit
Jiangnan Orogen

ABSTRACT

The northeastern Hunan Province hosts numerous hydrothermal Pb-Zn(-Cu-Co) polymetallic deposits. As a representative example, the Jingchong Cu-Co-Pb-Zn deposit is characterized by the lower Cu-Co and upper Pb-Zn mineralization, whereas little is known about Pb-Zn mineralization. In this study, three generations of sphalerite were identified based on their textural and geochemical differences. The Sph-I exhibits the oscillatory zoning that consists of reddish-brown Sph-Ia (poor in chalcopyrite inclusion) alternating with dark Sph-Ib with zoned chalcopyrite inclusion. Sph-II is composed of honey-brown Sph-IIa (abundant chalcopyrite droplets) and white clean Sph-IIb (rare chalcopyrite inclusion). The black Sph-III is characterized by nano- to submicron-sized chalcopyrite inclusions with typical "dusting" or "watermelon" texture and crosscuts all other sphalerite generations in veinlets. The electron microprobe and laser ablation inductively coupled plasma mass spectrometry show that Sph-I has higher Fe and Mn contents, but lower Cd, Cu and Ag contents than Sph-II and Sph-III. Sphalerite geothermometry yields temperatures of 334–346 (±58)°C for Sph-I, 254–289 (±60)°C for Sph-II and 286 (±55) °C for Sph-III. The sulfur fugacity ranges from $\log fS_2$ values of −9.03 to −8.26 for Sph-I to −11.77 to −10.63 for Sph-II and −10.82 for Sph-III. The combined textural features and chemical compositions indicate that the self-organized mechanism forms Sph-I, and that the coupled dissolution and precipitation reactions triggered by the influx of Cu-elevated fluids are responsible for the formation of Sph-II and Sph-III. The associated pyrite and pyrrhotite inclusions in sphalerite are produced by the exsolution mechanism, while chalcopyrite inclusions are formed by co-precipitation due to local supersaturation at the interface of sphalerite with fluid. The ^{40}Ar-^{39}Ar dating of muscovite in the Jingchong deposit yields a mineralizing age of ca. 121.1 ± 2 Ma, consistent with the ca. 130–120 Ma Pb-Zn mineralizing events in the northeastern Hunan Province. The sulfur isotopic values (−3.0 to +3.5‰) of the Pb-Zn ores are similar to that of Cu-Co ores, indicating a magmatic sulfur origin. Together with the trace element affinity of sphalerite with magmatic-hydrothermal origin, it was proposed that the Jingchong Pb-Zn and Cu-Co mineralization were formed in the same magmatic-hydrothermal system. The placement of Pb-Zn orebodies at the upward zoning of Cu-Co orebodies could be attributed to the higher solubilities of Pb and Zn chloride complexes in hydrothermal fluids, relative to Cu chloride complex.

1. Introduction

Sphalerite is the most important zinc mineral in a variety of zinc sulfide deposits (Cook et al., 2009; Ye et al., 2011). Significant amounts of minor and trace elements like Mn, Fe, Co, Ni, As, Cu, Ga, Ge, Se, Mo, Ag, Cd, In, Sn, Sb, Hg, Tl, Pb and Bi are incorporated into sphalerite as

---

* Corresponding author.
E-mail address: wangzhilin1025@163.com (Z. Wang).

https://doi.org/10.1016/j.oregeorev.2023.105667
Received 23 June 2023; Received in revised form 24 August 2023; Accepted 12 September 2023

Fig. 1. **a** Tectonic framework of the South China Block showing location of the Jiangnan Orogen in WSG 84 (modified after Zhao, 2015). **b** Geological map of northeastern Hunan Province in WSG 84 (modified after Xu et al., 2009).

solid solution and/or mineral inclusions at sub-ppm to weight-percent levels, which is dependent on the crystallization temperature, pressure, pH, redox potential, fluid chemistry and mineral assemblages (Cook et al., 2009; Ye et al., 2011; Belissont, 2014; Bonnet et al., 2016; Frenzel et al., 2016; George et al., 2016; Zhuang et al., 2019; Zhu et al., 2021; Luo et al., 2022). Thus, the element composition of sphalerite can be used to constrain the physical and chemical conditions of the ore-forming fluid and even the ore deposit type (Barton and Bethke, 1987; Keith et al., 2014; Frenzel et al., 2016, 2022). For instance, sphalerite preferentially incorporates Fe, Mn and In in high-temperature magmatic-hydrothermal systems which are characterized by low oxygen fugacity. Conversely, the enrichment of Ga, Ge, Tl and As in sphalerite occurs in sediment-hosted deposits with relatively low temperature, i.e. Mississippi valley-type deposits (Cook et al., 2009; Belissont, 2014; Frenzel et al., 2016; Zhou et al., 2018). In addition, the intergrowth of sphalerite and various mineral inclusions such as chalcopyrite, pyrrhotite and pyrite have been explained by exsolution, co-precipitation, or replacement mechanisms (Kojima and Sugaki, 1987; Bortnikov et al., 1991; Nagase and Kojima, 1997; ÇiFtçï, 2011; Govindarao et al., 2018). Therefore, the combined features of mineral assemblage, textures and chemical compositions of sphalerite and associated mineral inclusions can help understand the Pb-Zn mineralizing process (Ramdohr, 1969; Cook et al., 2009; Ye et al., 2011; Cugerone et al., 2020).

The Yanshanian (150–120 Ma) is an important period of large-scale Au, Cu, Co, Pb and Zn mineralization in South China (Hua et al., 2005; Mao et al., 2011; Chen, 2014; Deng et al., 2017, 2020; Xu et al., 2017, 2022; Zou et al., 2018). The northeastern Hunan Province, located in the central segment of the Jiangnan Orogen, South China, hosts different types of Pb-Zn deposits, such as the hydrothermal vein-type Jingchong and Hengdong Cu-Co-Pb-Zn deposits (Wang et al., 2017, 2022; Zou et al., 2018), hydrothermal vein-type Taolin and Lishan Pb-Zn deposits (Yu et al., 2020, 2021; Guo et al., 2018) and skarn-porphyry type Qibaoshan and Aoyushan Cu-Pb-Zn deposits (Liu, 2017; Yuan et al., 2018). Particularly, these deposits are accompanied by some critical metal resources, as represented by Co in the Jingchong and Hengdong deposits (Wang et al., 2017, 2022; Zou et al., 2018), Ga and Se in the Taolin and Lishan deposits, and In in the Qibaoshan deposit (Liu, 2017). These hydrothermal vein-type deposits share similar ore-forming features such as orebodies controlled by fracture zones or faults and the close tempo-spatial correlation with the Jurassic-Cretaceous granitoids (i.e., orebodies either occurring within or approaching the Jurassic-Cretaceous granitoids) (Wang et al., 2017; Yu et al., 2020, 2021). However, there are still differences in ore geology. For example, fluorite and barite are the main gangue minerals in the Taolin and Lishan Pb-Zn deposits (Yu et al., 2020, 2021), instead, the Jingchong Cu-Co-Pb-Zn deposit has quartz as the main gangue mineral (Wang et al., 2017, 2022). As a result of little attention to the Pb-Zn mineralization in the Cu-Co-Pb-Zn system, it is unclear about the discrepancy among these deposits.

The Jingchong Cu-Co-Pb-Zn deposit with reserves of 0.24 Mt Cu, 3718 t Co, 12250 t Pb and 72831 t Zn, is characterized by lower Cu-Co and upper Pb-Zn orebodies (Wang et al., 2017, 2022). Previous studies focus on the Cu-Co metallogeny and interpreted that the deposit has a magmatic-hydrothermal provenance according to sulfur, lead, helium and argon isotopic analyses (Ning, 2002; Yi et al., 2010; Wang et al., 2017). Field investigation and detailed mineralogy reveal that cobaltiferous pyrite (up to 13.66 wt% Co) and cobaltite-alloclasite are responsible for Co mineralizing stage which follows the Cu stage and, in turn, followed by the Pb-Zn stage (Wang et al., 2022). However, little is known about the formation conditions of Pb-Zn ores and its correlation with Cu-Co mineralization, which limit understanding of the Cu-Co-Pb-Zn mineralizing process.

Sphalerite in the Jingchong deposit exhibits various mineralogical characteristics (e.g., diverse color, texture and mineral inclusions), indicating complex growth mechanisms and varying ore-forming

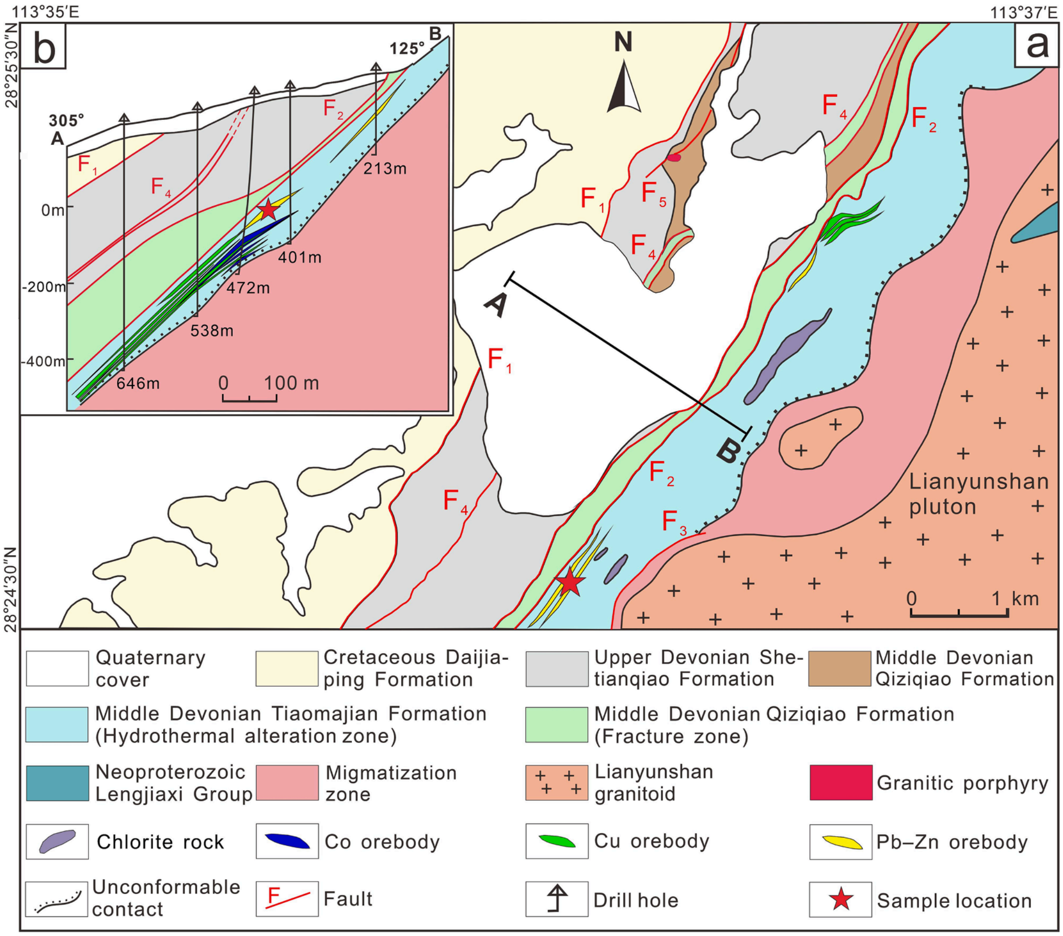

Fig. 2. **a** Simplified geological map of the Jingchong Cu-Co-Pb-Zn deposit in WSG 84 (modified after Wang et al., 2017). **b** Exploration section along line A–B showing the occurrence of Cu-, Co- and Pb-Zn orebodies (modified after Wang et al., 2017).

conditions during Pb-Zn mineralization. Here, we present data on sphalerite texture and chemical composition determined by *in-situ* electron probe microanalyzer (EPMA) and Laser ablation inductively coupled plasma mass spectrometry (LA-ICP-MS), with special attention to the elemental distribution of Fe, Mn, Cd, Cu, Ag, In and Ga. Principal component analysis, sphalerite geothermometry and fS_2 calculation are used to describe element substitution mechanisms and the formation conditions associated with sphalerite generations. Furthermore, *in-situ* sulfur isotope data of sphalerite are used to constrain the source of ore-forming fluids. In combination with muscovite $^{40}Ar/^{39}Ar$ dating, the Pb-Zn mineralizing process and its correlation with the Jingchong Cu-Co mineralization are elaborated.

2. Regional geology

The South China Block is composed of two tectonic units: the Cathaysia Block to the southeast and the Yangtze Block to the northwest (Fig. 1a). These two continental blocks collided in the Neoproterozoic and formed the Jiangnan Orogen (Charvet et al., 1996, 2010; Li, 1999; Zhou et al., 2002a, 2002b; Wang et al., 2007, 2014a; Yao et al., 2014; Zhao, 2015). The Neoproterozoic successions include the early to middle Neoproterozoic Lengjiaxi Group and the middle Neoproterozoic Banxi Group (Zhao and Cawood, 2012; Wang et al., 2016). The Lengjiaxi Group is a suite of flysch turbidites mainly composed of sandstone, siltstone and pelite in protolith intercalated with volcanic rocks deposited in *retro*-arc foreland basins or in the back-arc at ca. 860–820 Ma (Wang et al., 2007, 2014a; Wang et al., 2010, 2012, 2013; Gao et al., 2011). The Banxi Group overlying the Lengjiaxi Group by an angular unconformity is mainly composed of sandstone, conglomerate and pelite with subordinate carbonate and volcanic rocks formed at ca. 800–760 Ma in a rift and passive margin environment (Wang et al., 2007, 2010).

The northeastern Hunan Province is located at the central segment of the Jiangnan Orogen. The Neoproterozoic successions (dominantly including the Lengjiaxi and Banxi groups metamorphosed in the greenschist facies) and Meso to Cenozoic red-bed rocks together with minor Archean to Paleoproterozoic crystalline metamorphic rocks (the Lianyunshan and Jianxichong groups) and Paleozoic sedimentary rocks constitute the lithostratigraphic units in this region (Wang et al., 2017; Zhou et al., 2021). Magmatism from the Neoproterozoic to the Jurassic-Cretaceous occurred in this area (Li, 2000; Mao et al., 2011; Lin et al., 2022), of which the Jurassic-Cretaceous granitoids are the most widespread (Fig. 1), including the Mufushan pluton (ca. 154–127 Ma; Wang et al., 2014b; Xu et al., 2022), Wangxiang pluton (ca. 160–140 Ma), Jinjing pluton (ca. 160–145 Ma) and the Lianyunshan pluton (ca. 155–140 Ma; Wang et al., 2016; Ji et al., 2017; Deng et al., 2017). The structural framework is characterized by two horsts and three grabens, namely the Miluo graben, the Mufushan–Wangxiang horst, the Changsha–Pingjiang graben, the Liuyang–Hengdong horst and the Liling–Youxian graben, from northwest to southeast (Xu et al., 2009). Several NE-trending, crustal-scale faults, represented by the Xinning–Huitang and the Changsha–Pingjiang fault zones form the major structures (Fig. 1b). Abundant Au-, Cu-Co-Pb-Zn- and Nb-Ta-Li deposits occur in the Mufushan–Wangxiang and Liuyang–Hengdong horsts (Fig. 1b).

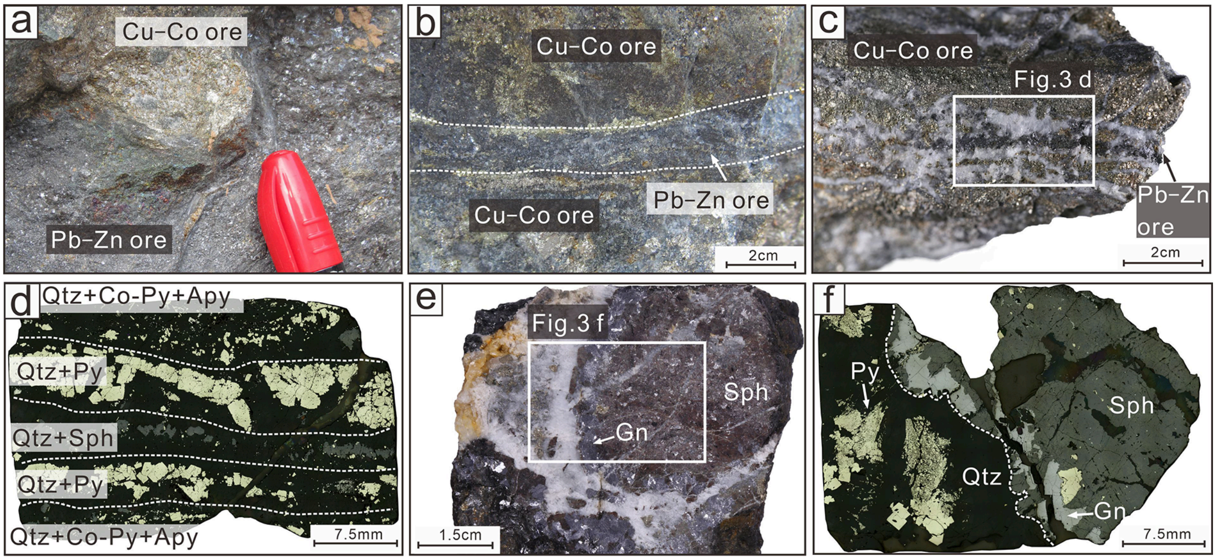

Fig. 3. Photographs showing the occurrences of Pb-Zn ores from the Jingchong deposit. **a** Pb-Zn ore has a clear boundary with the Cu-Co ore. **b** Pb-Zn veinlets crosscut Cu-Co ore. **c** Quartz-sphalerite veinlets crosscut the Cu-Co ore. **d** Pb-Zn veinlet crosscuts the early-formed Cu-Co ore consisting of alternated Qtz + Co-rich pyrite + arsenopyrite and Qtz + pyrite; reflected light. **e** Pb-Zn ore was crosscut by the barren quartz veinlets with breccias of early Cu-Co- and Pb-Zn ores. **f** reflected light of Fig. e. Mineral abbreviations: Py, pyrite; Co-Py, Co-rich pyrite; Sph, sphalerite; Gn, galena; Qtz, quartz; Apy, arsenopyrite.

3. Deposit geology

The Jingchong Cu-Co-Pb-Zn deposit, situated at the contact of the Changsha–Pingjiang graben and the Liuyang–Hengdong horst, is controlled by the regional Changsha–Pingjiang fault zone (Fig. 1b). This fault zone stretches for nearly 680 km and experienced the transform from transpression to transtension during the Jurassic to the Early Cretaceous (Zhou et al., 2021). It consists of numerous NE-trending parallel faults labeled by $F_{1\text{-}5}$, of which F_2 is the main fault with a width of 10–100 m, a strike of N30°E and 40° NW dip (Fig. 2a).

The lithostratigraphic units comprise the Neoproterozoic Lengjiaxi Group, the Middle Devonian Tiaomajian and Qiziqiao formations, the upper Devonian Shetianqiao Formation, the Cretaceous Daijiaping Formation and the Quaternary sediments (Fig. 2a). Due to the intrusion of the Lianyunshan granitoid, the Lengjiaxi Group to the east of the mining area occurs as the migmatization zone with the width of 15–240 m which consists of grey to dark-green banded migmatites and migmatitic gneiss. Fragments of the Lengjiaxi Group form as inclusion in the Lianyunshan granitoid. With the unconformity or fault contact with the Neoproterozoic Lengjiaxi Group, the Devonian Tiaomajian Formation with the lithological protolith of argillaceous limestone, shale, sandy shale, quartz sandstone and conglomerate occur at the footwall of F_2. The Devonian Qiziqiao Formation occurs in the hanging wall of F_2 and comprises limestone, dolomite, dolomitic limestone and calcareous slate. Due to faulting and hydrothermal activity, the Tiaomajian and Qiziqiao formations have been modified to the hydrothermal alteration zone and fracture zone, respectively (Fig. 2a). The hydrothermal alteration zone is characterized by silicified and/or chloritized breccia and quartzite. The fracture zone is comprised of cataclasite and gouge. The Devonian Shetianqiao Formation occurs in the centre of the mining area and mainly consists of slate and minor sandstone lenses. To the west, the Cretaceous Daijiaping Formation consists of purple-red sandstone, slate and sandy conglomerate. Quaternary sediments cover all other lithologies unconformably.

Magmatism is represented by the Late Jurassic to the Early Cretaceous Lianyunshan granitoid. It is mainly composed of biotite monzogranite, two mica monzogranite and granodiorite. In addition, minor granite porphyry occurs along F_5 (Ning, 2002), although no age data are available.

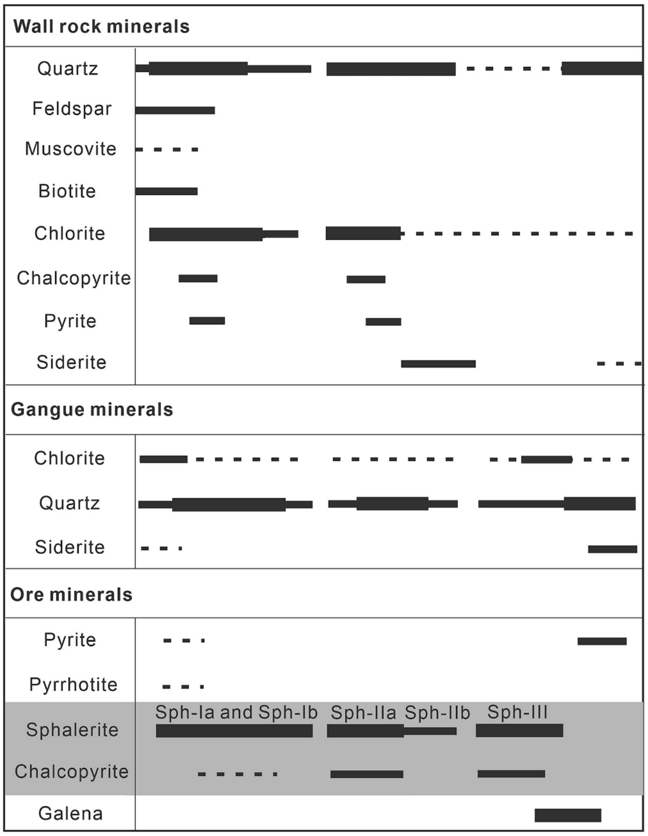

Fig. 4. Simplified paragenetic mineral sequences of the Pb-Zn mineralization in the Jingchong deposit.

Orebodies mainly occur as lenticular veins surrounded by the hydrothermal alteration zone, with Pb-Zn orebodies at the upper part of the hydrothermal alteration zone and Cu-Co orebodies in the lower segment (Fig. 2b). The Cu-Co orebodies are described by Wang et al. (2022), thus only Pb-Zn orebodies are introduced here. They are mainly present as veins and have a strike parallel to that of the hydrothermal alteration zone. Locally, it can be observed that Pb-Zn veinlets crosscut the Cu-Co ores (Fig. 3a-d), and the barren quartz veinlets crosscut Pb-Zn ores (Fig. 3e and f). The Pb-Zn ores have euhedral to anhedral granular, cataclastic and replacement textures, with vein, veinlet and massive structures (Fig. 3c-f). The ore mineral assemblage includes sphalerite and galena, with minor chalcopyrite, pyrite and pyrrhotite. The gangue minerals dominantly consist of quartz, with minor chlorite and siderite (Fig. 4).

4. Sampling and analytical methods

Nine representative Pb-Zn ore samples were collected from underground at 50 m and 0 m elevations (Table ESM 1). These samples include four samples from vein ores (05-B1, 05-B2, 05-B3, 05-B4) and five samples from massive ore (55B-B1, 55B-B2, 59-B2, 5B-4-1-1B, 5B-6-4-1B). They were prepared as polished thin sections for mineral chemistry and sulfur isotope analyses based on petrographic observation. In addition, one altered rock sample (JC-12 ms) with sphalerite mineralization from the hydrothermal alteration zone was selected for muscovite $^{40}Ar/^{39}Ar$ dating.

4.1. Electron probe microanalyzer (EPMA)

Major and selected trace elements of sphalerite were determined using the SHIMADZU EPMA-1720 electron microprobe equipped with four wavelength-dispersive spectrometers (WDS) at the School of Geosciences and Information Physics, Central South University, China. EPMA uses an accelerating voltage of 20 kV, a beam current of 10 nA and a beam diameter of 1 μm (Table ESM 2). The following elements, analytical lines, standards and monochromators were used for spot analysis: S (Kα, ZnS, PET), Zn (Kα, ZnS, LIF), Fe (Kα, FeS_2, LIF), Co (Kα, Co, LIF), Ni (Kα, Ni, LIF), Cu (Kα, Cu, LIF), Cd (Lα, Cd, PET), Ga (Lα, GaAs, TAP), Ge (Lα, Ge, TAP), Sn (Lα, Sn, PET) and Pb (Mα, PbS, PET). The ZAF method (Duncumb and Reed, 1968) was used for the correction of matrix effects. In addition, Fe (Kα, LIF), Zn (Kα, LIF) and Cu (Kα, LIF) were selected for EPMA element mapping, with an acceleration voltage of 20 kV, beam current of 50 nA, sampling time for each point ranging from 30 to 80 ms, beam size of 1 μm and pitch of 1.1 μm. A total of 143 EPMA spot analyses were carried out for the three sphalerite generations (Table ESM 3).

4.2. Laser ablation inductively coupled plasma mass spectrometry (LA-ICP-MS)

Minor and trace element concentrations in sphalerite were determined by a Teledyne Cetac HE 193 nm laser ablation system linked to an Analytik Jena Plasma Quant MS Ellite ICP-MS at the School of Geoscience and Information Physics, Central South University, China (Batch 1 and 2, Table ESM 4) and a Teledyne 193 nm Excimer Laser coupled to an Element XR Thermo Fisher ICP-MS at the Laboratory of Environmental and Raw Materials Analysis (LERA), Karlsruhe Institute of Technology, Germany (Batch 3, Table ESM 4). Measurements at the Central South University were operated at a constant pulse rate of 5 Hz and an energy density of 2.5 J/cm^2 with the spot size of 35 μm. Each analysis comprises 20 s of background measurement and 40 s of sample ablation, followed by a 20 s retention time to ensure proper cell washout. The following isotopes were monitored: ^{32}S, ^{55}Mn, ^{57}Fe, ^{59}Co, ^{60}Ni, ^{63}Cu, ^{66}Zn, ^{69}Ga, ^{73}Ge, ^{75}As, ^{78}Se, ^{95}Mo, ^{107}Ag, ^{111}Cd, ^{115}In, ^{118}Sn, ^{121}Sb, ^{125}Te and ^{205}Tl with dwell times of 10 ms for each element. External calibration was performed with the synthetic polymetallic sulfide standards MASS-1 (Wilson et al., 2002) as the primary reference material. The synthetic basaltic glass GSE-2G (Wilson, 2019) and standard glasses NIST SRM610 and NIST SRM612 (Pearce et al., 1997) were measured to check for instrumental drift. The analysis in LERA was done with a spot size of 35 μm, laser frequency of 10 Hz and fluence of 5 J/cm^2. The ^{32}S, ^{55}Mn, ^{57}Fe, ^{59}Co, ^{60}Ni, ^{63}Cu, ^{66}Zn, ^{69}Ga, ^{72}Ge, ^{73}Ge, ^{75}As, ^{78}Se, ^{95}Mo, ^{107}Ag, ^{111}Cd, ^{113}In, ^{115}In, ^{118}Sn, ^{121}Sb, ^{125}Te, ^{205}Tl, ^{208}Pb and ^{209}Bi were measured with 16 ms of dwell time separately. Calibrations were conducted using the sulfide pressed-pellets Fe-S_1, Fe-S_4, Fe-S_5 from UQAC University (Savard et al., 2018), and basaltic glasses BHVO-2, BCR-2 (Jochum et al., 2016) and standard glasses NIST SRM612 (Pearce et al., 1997) from the USGS. The concentrations of elements in both measurements were calculated using the Iolite 4 (Paton et al., 2011) and the limits of detection (LOD) for each analysis were calculated using the methods described by Pettke et al. (2012). In the data reduction process, we pay special attention to Fe signals in LA-ICP-MS time-resolved depth profiles given that Fe is the major element of chalcopyrite, pyrite and pyrrhotite inclusions, and has less interference from background noises due to relatively high Fe contents in the Jingchong sphalerite. The jagged sections of the time-resolved depth profiles (especially for Fe signals) were omitted and only the smooth sections that last at least 20 s were integrated into the measurement interval. As a result, the measurements provide credible information about element concentrations in sphalerite. Corresponding EPMA-determined average Zn concentrations were utilized as internal standards for different sphalerite varieties. Indium concentrations were corrected for the isobaric interference of ^{115}Sn on ^{115}In and ^{113}Cd on ^{113}In, and ^{115}In results were used based on relative high Cd and low Sn contents in Jingchong sphalerite. The complete LA-ICP-MS dataset (concentration, quality control and limit of detection) is provided in the electronic supplementary material (Tables ESM 4 and 5). The data quality control results show that all three data batches are comparable and robust. A total of 154 LA-ICP-MS spot analyses were carried out for the three sphalerite generations (Table ESM 4).

LA-ICP-MS elemental mapping was performed at the Central South University with an energy density of 2 J/cm^2, spot size with 30 μm and repetition rate of 5 Hz. Reference material (MASS-1) was measured at the start and end of the mapping using the same settings. The mapping images were processed using in-house software (Wang et al., 2017). It is notable that the element maps cannot be corrected for isotopic interferences.

4.3. Laser ablation multi-collector inductively coupled plasma mass spectrometry (LA-MC-ICP-MS)

In-situ sulfur isotopic studies on sphalerite and coexisting pyrite were performed at Nanjing FocuMS Technology Co. Ltd. (China) utilizing a Teledyne Cetac Technologies Analyte Excite laser-ablation system in conjunction with a Nu Instruments Nu Plasma II MC-ICP-MS. Spot measurements were performed using a 30 μm beam size for pyrite and a 40 μm beam size for sphalerite, a pulse rate of 5 Hz, and a laser energy of 100 mJ. After four spot analyses, natural pyrite Wenshan (WS-1; $\delta^{34}S_{V\text{-}CDT} = +1.1‰ \pm 0.2‰$; Zhu et al., 2017) was measured as an external standard. The pressed powder pellets of pyrite GBW 07267 ($\delta^{34}S_{V\text{-}CDT} = +3.6‰ \pm 0.3‰$; Fu et al., 2016) and chalcopyrite GBW 07268 ($\delta^{34}S_{V\text{-}CDT} = -0.3‰ \pm 0.3‰$; Fu et al., 2016) from China's National Research Center for Geoanalysis as well as fine-grained sphalerite NBS 123 ($\delta^{34}S_{V\text{-}CDT} = +17.8‰ \pm 0.2‰$; Bao et al., 2017) from the United States National Institute of Standards and Technology were used for quality control. Sulfur isotope compositions are expressed in terms of Canyon Diablo Troilite in conventional notation (CDT). The repeatability of the results was better than 0.6‰ (1σ). Results are given in the electronic supplementary material (Table ESM 6). Thirty-eight *in-situ* sulfur isotope analyses of sphalerite and associated pyrite were summarized in Fig. 11 and Table ESM 6.

4.4. Statistical analysis

Principal component analysis (PCA) as multivariate statistical analysis is commonly used to reveal the most relevant trends based on a geochemistry dataset without external supervision (Belissont, 2014; Frenzel et al., 2016; Bauer et al., 2019; Yu et al., 2020). Here, we apply PCA to determine the relevance of important minor and trace elements

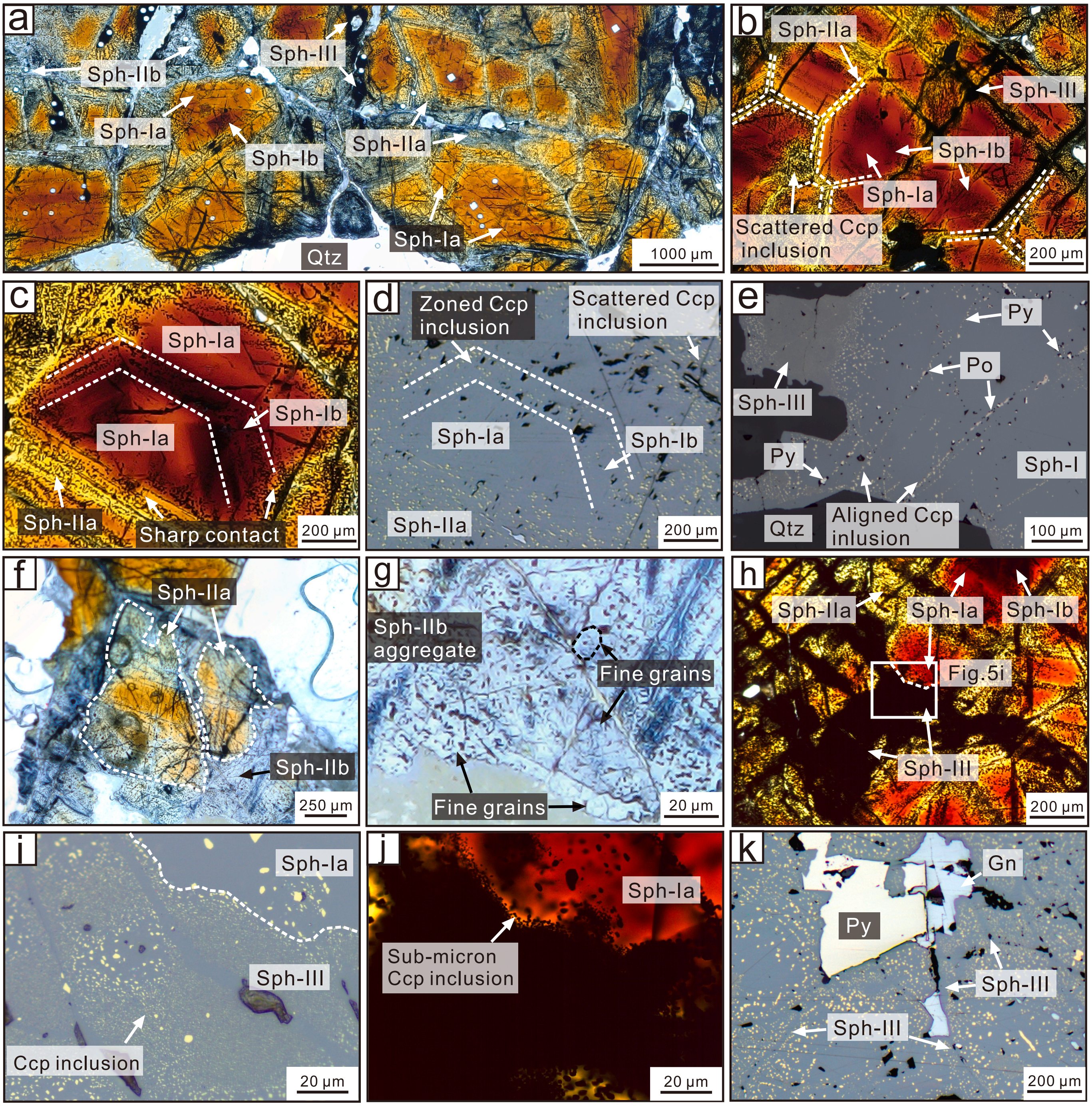

Fig. 5. Photomicrographs showing mineral assemblages of Pb-Zn ores and sphalerite textures from the Jingchong deposit. **a** Sph-I comprises reddish-brown Sph-Ia bands alternating with dark Sph-Ib bands. The honey-brown Sph-IIa replaces Sph-I, in turn is overgrown by white Sph-IIb. The black Sph-III crosscuts other sphalerite types. The white round and square-shaped dots are pits after laser ablation; transmitted light. **b** Sph-IIa formed along the grain boundaries (in white dash line) of Sph-I relics; transmitted light. **c-d** Sph-Ib are characterized by zoned chalcopyrite inclusions which are distributed along the crystal plane. Sph-IIa contains chalcopyrite blebs distributed unevenly and has sharp contact with Sph-I. **c**, transmitted light; **d**, reflected light. **e** Aligned pyrrhotite, chalcopyrite and pyrite inclusions in Sph-I. Noting Sph-III with dusting chalcopyrite inclusions cutting Sph-I; reflected light. **f** White Sph-IIb postdates Sph-IIa as the outer rim in an epitaxial texture; transmitted light. **g** Sph-IIb locally occurs as fine-grained aggregates; transmitted light. **h** Sph-III veinlets crosscut Sph-I and Sph-II along fractures; transmitted light. **i** Corresponding zoomed area of **h.** Sph-III is rich in submicron chalcopyrite inclusions which are present as typical "dusting" or "watermelon" texture; reflected light. **j** Transmitted light of **i**. **k** Galena and pyrite coexisting with Sph-III; reflected light.

in sphalerite. Raw trace element data are log-transformed to ensure the approximate normality required for statistical treatment and are processed by the ioGAS software through the PCA function. Only the elements in more than half of all cases with concentrations above the detection limit were selected for calculation, and the concentrations below the detection limits in the dataset were replaced by random numbers in the normal distribution with a mean and standard deviation equal to the corresponding detection limit (Frenzel et al., 2016).

4.5. Muscovite $^{40}Ar/^{39}Ar$ dating

After crushing and sieving to 250 to 500 μm size, muscovite was

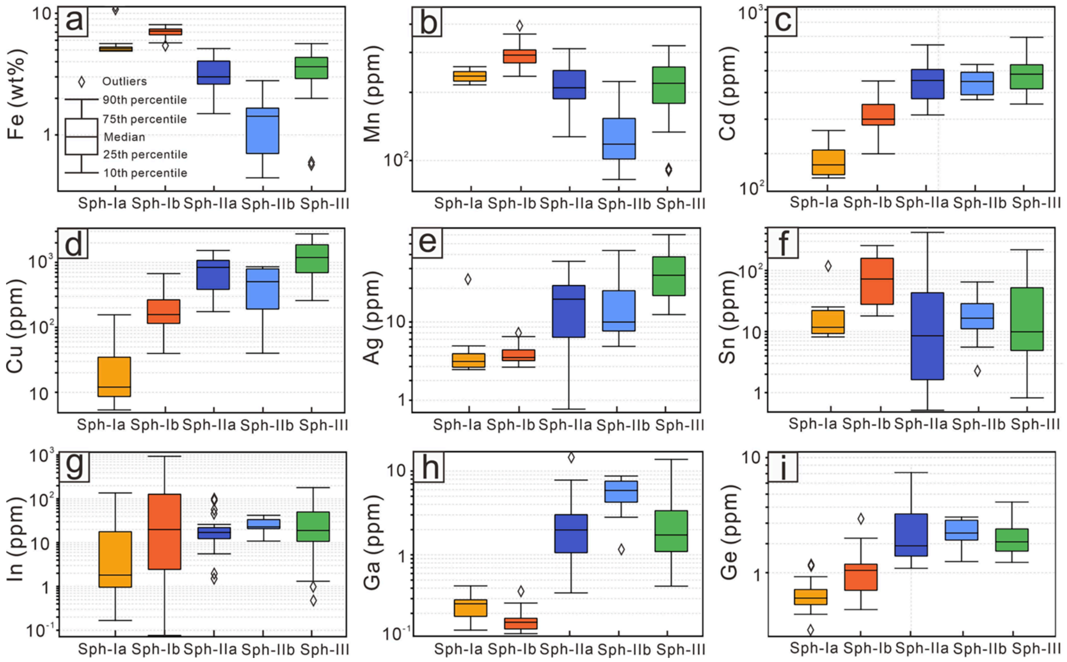

Fig. 6. Box-and-whisker plots of the major and trace element contents of different sphalerite species from the Jingchong deposit. Iron (wt%) is from EPMA analyses and other trace elements (ppm) are from LA-ICP-MS analyses.

handpicked under a binocular with > 99% purity. For further purification, muscovite is cleaned with nitric acid to remove carbonates and then washed with deionized water. After drying in an oven at 105 °C for 15 h, muscovite separates and the monitor sample ZBH-2506 (Beijing Fangshan granodiorite biotite, ca. 132.7 ± 0.5 Ma; Wang, 1983) were irradiated together in the 49-2 reactor at the atomic reactor of the Research Institute of Atomic Energy (Beijing, China) for an irradiation time of 23 h and 44 min. After cooling, the samples were placed in a sample holder, sealed and degassed, and then analyzed by the $^{40}Ar/^{39}Ar$ step-heating method by an Argus VI static vacuum mass spectrometer at the Key Laboratory of Tectonics and Petroleum Resources, Ministry of Education, University of Geosciences (Wuhan), China. The correction factors include $(^{39}Ar/^{37}Ar)_{Ca} = 0.000852$, $(^{36}Ar/^{37}Ar)_{Ca} = 0.000278$ and $(^{40}Ar/^{39}Ar)_{Ca} = 0.001147$. The $^{40}Ar/^{39}Ar$ results were processed and plotted using the ArArCALC Version 2.40 software (Koppers, 2002), and the decay constant used for calculations was $\lambda = (5.543 \pm 0.010) \times 10^{-10} a^{-1}$ (Steiger and Jäger, 1977). The detailed analytical procedure is described by Qiu et al. (2010) and Zhang et al. (2014). The $^{40}Ar/^{39}Ar$ data are summarized in Table ESM 7.

5. Results

5.1. Sphalerite mineralogy and paragenesis

Based on the texture and distribution pattern of mineral inclusions, three sphalerite generations and five sphalerite subtypes are distinguished in the Jingchong deposit (Fig. 5a-d).

The first sphalerite generation (Sph-I) forms idiomorphic grains and is characterized by oscillatory zoning that consists of reddish-brown (Sph-Ia) alternated with dark (Sph-Ib) zones (Fig. 5b-d). The reddish-brown Sph-Ia zone is poor in chalcopyrite inclusion, while the dark Sph-Ib is featured by zoned chalcopyrite inclusions (Fig. 5d). In addition, pyrite and pyrrhotite blebs, ellipsoids or lamella are locally present as mineral inclusions within Sph-Ia and Sph-Ib (Fig. 5e). Due to fractures, Sph-I grains are commonly preserved as relics (Fig. 5a-c).

The second sphalerite generation (Sph-II) generally replaces or overgrows Sph-I and is further divided into two sub-types based on color and texture. The Sph-IIa is honey-brown and was formed along the cleavage, fracture or grain boundary of Sph-I (Fig. 5a-c). Abundant chalcopyrite droplets are unevenly distributed in Sph-IIa (Fig. 5b-d). Relatively, white Sph-IIb typically postdates Sph-IIa as outer rims in an epitaxial texture (Fig. 5f) or occurs as fine-grained mineral aggregates (Fig. 5g). Chalcopyrite inclusions are rarely found in the Sph-IIb (Fig. 5f, g).

In contrast to Sph-I and Sph-II, the third sphalerite generation (Sph-III) is opaque. The Sph-III generally occurs along fractures and crosscuts all early sphalerite generations in healed or unhealed veinlets (Fig. 5a, b, h, i). Nano- to submicron-sized zoned chalcopyrite inclusions are widespread in Sph-III, which is commonly referred to as a “dusting” or “watermelon” texture (Fig. 5i, j) (Bortnikov et al., 1991; Bente and Doering, 1995; Seifert and Sandmann, 2006; Cook et al., 2009). Noticeably, these inclusions become gradually denser and smaller in size as they are closer to fractures (Fig. 5i, k). Locally, anhedral galena and pyrite occur with Sph-III (Fig. 5k).

5.2. Sphalerite chemical compositions and geothermometry and sulfur fugacity

Sph-I has a relatively broad compositional spectrum due to the oscillatory zoning. Generally, Sph-Ia has higher Zn (54.97–63.10 wt%) but lower Fe (3.57–11.32 wt%) contents than Sph-Ib (56.16–57.77 wt% Zn, 8.32–9.78 wt% Fe; Table ESM 3). The average formulae are $(Zn_{0.869}, Fe_{0.128})S$ for Sph-Ia and $(Zn_{0.839}, Fe_{0.160})S$ for Sph-Ib. Sph-Ib is enriched in In (0.08–947 ppm), Cu (40.1–679 ppm) and Sn (17.6–250 ppm) relative to Sph-Ia (0.17–136 ppm In, 5.4–158 ppm Cu, 0.87–117 ppm Sn). Sph-Ib also has slightly higher Mn (236–394 ppm), Cd (299–550 ppm), Ag (3.88–7.82 ppm), Ga (0.10–0.36 ppm) and Ge (0.52–2.69 ppm) contents than Sph-Ia (216–260 ppm Mn, 245–364 ppm Cd, 3.77–25.4 ppm Ag, 0.07–0.43 ppm Ga, 0.36–1.12 ppm Ge). In contrast, Sph-II has lower Fe but higher Cd, Cu and Ag contents than Sph-I (Fig. 6a, c, d, e). In Sph-II, Sph-IIa has Fe (0.58–6.10 wt%) contents higher than that of Sph-IIb (0.59–1.44 wt%), and the corresponding average formulae are $(Zn_{0.940}, Fe_{0.056})S$ for Sph-IIa and $(Zn_{0.981}, Fe_{0.017})S$ for Sph-IIb. Besides, Sph-IIa has higher Mn (127–312 ppm) and Cu (175–1530 ppm) contents than Sph-IIb (82.4–223 ppm Mn, 40.0–858 ppm Cu). The In (1.27–128 ppm) and Ga (0.35–15.1 ppm) contents in

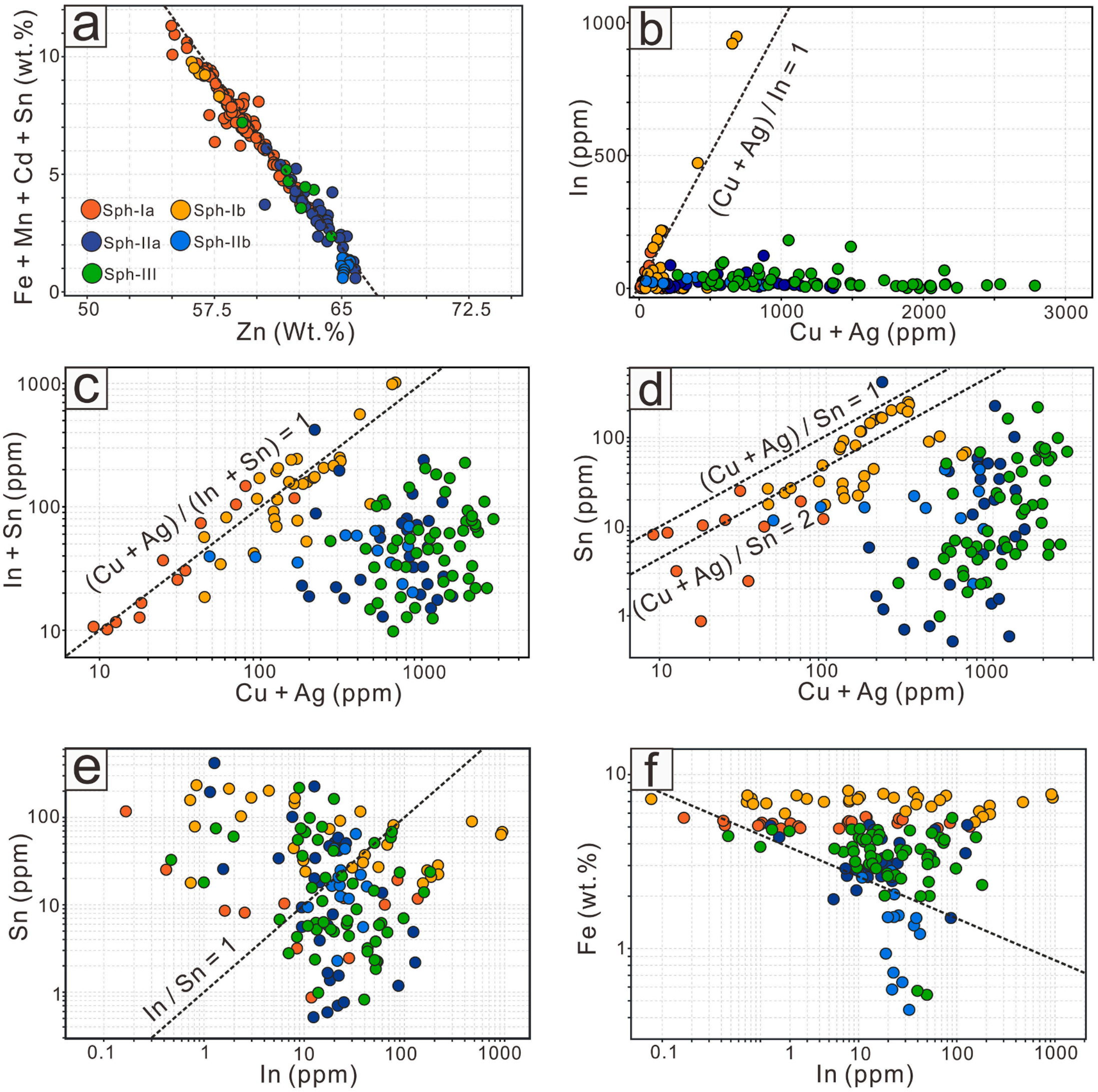

Fig. 7. Bivariate plots of Zn vs. Fe + Mn + Cd + Sn (**a**), Cu + Ag vs. In (**b**), Cu + Ag vs. In + Sn (**c**), Cu + Ag vs. Sn (**d**), In vs. Sn (**e**), and In vs. Fe (**f**).

Table 1
GGIMFis temperature, $\log_{10}$(FeS), and $\log_{10}(fS_2)$ values (arithmetic means ± 2 σ).

Generation	PC1	$T_{GGIMFis}$ (°C)	2 $\sigma_{external}$ (°C)	$\log_{10}$(FeS) (mol.%)	$\log_{10}(fS_2)$	2 $\sigma_{external}$ (fS_2)
Sph-Ia	−2.32 ± 0.14	334 ± 7	±56	−0.58 ± 0.01	−9.03 ± 0.01	±0.03
Sph-Ib	−2.54 ± 0.12	346 ± 6	±58	−0.49 ± 0.01	−8.26 ± 0.02	±0.06
Sph-IIa	−1.50 ± 0.12	289 ± 7	±55	−0.76 ± 0.03	−10.63 ± 0.07	±0.19
Sph-IIb	−0.84 ± 0.18	254 ± 10	±60	−1.05 ± 0.1	−11.77 ± 0.20	±0.38
Sph-III	−1.44 ± 0.09	286 ± 5	±55	−0.73 ± 0.04	−10.82 ± 0.08	±0.29

Note: Uncertainties provided here for PC1*, $T_{GGIMFis}$, $\log_{10}$(FeS), and $\log_{10}(fS2)$ in the corresponding columns are internal uncertainties. External uncertainties described by 2 $\sigma_{external}$ in separate columns contain all sources of uncertainty. The uncertainty levels correspond to ±2 standard errors in all cases.

Sph-IIa vary greatly relative to that of Sph-IIb (10.9–42.2 ppm In, 1.15–8.72 ppm Ga). The concentrations of Cd and Ge show no significant differences between the two sub-types (Fig. 6 c, i). The Sph-III contains moderate amounts of Fe (2.36–7.20 wt%), with the average formula of $(Zn_{0.915}, Fe_{0.078})S$. In contrast to Sph-I and Sph-II, Sph-III has the highest contents of Cd (454–794 ppm), Cu (259–2748 ppm) and Ag (11.6–60.3 ppm). The concentrations of Sn and In are variable, ranging from 0.82 to 218 ppm and 0.47–181 ppm, respectively. The contents of Mn, Ga and Ge are 89.6–321 ppm, 0.42–13.8 ppm and 1.22–3.67 ppm, respectively (Fig. 6). The Ni, As, Se, Mo, Sb, Te, Au and Tl contents are generally low (Table ESM 4). Binary plots are used to discriminate the correlation between elements in Jingchong's sphalerite. In Fig. 7, a clear negative correlation is seen between the element groups of Zn and Fe + Mn + Cd + Sn, whereas positive correlations are observed in the plots of Cu + Ag vs. In, Cu + Ag vs. In + Sn, Cu + Ag vs. Sn, and In vs. Sn. The In content, however, tends to increase with decreasing Fe content in sphalerite (Fig. 7f).

The GGIMFis geothermometer is employed to estimate the formation temperature of sphalerite varieties according to the Ga, Ge, Fe, Mn and In contents (Frenzel et al., 2016). The calculated formation temperature for the five sphalerite varieties is given in Table 1. Specifically, the GGIMFis geothermometer gives average temperatures of 334 ± 56 °C for Sph-Ia, 346 ± 58 °C for Sph-Ib, 289 ± 55 °C for Sph-IIa, 254 ± 60 °C for Sph-IIb, and 286 ± 55 °C for Sph-III (Table 1). Based on GGIMFis

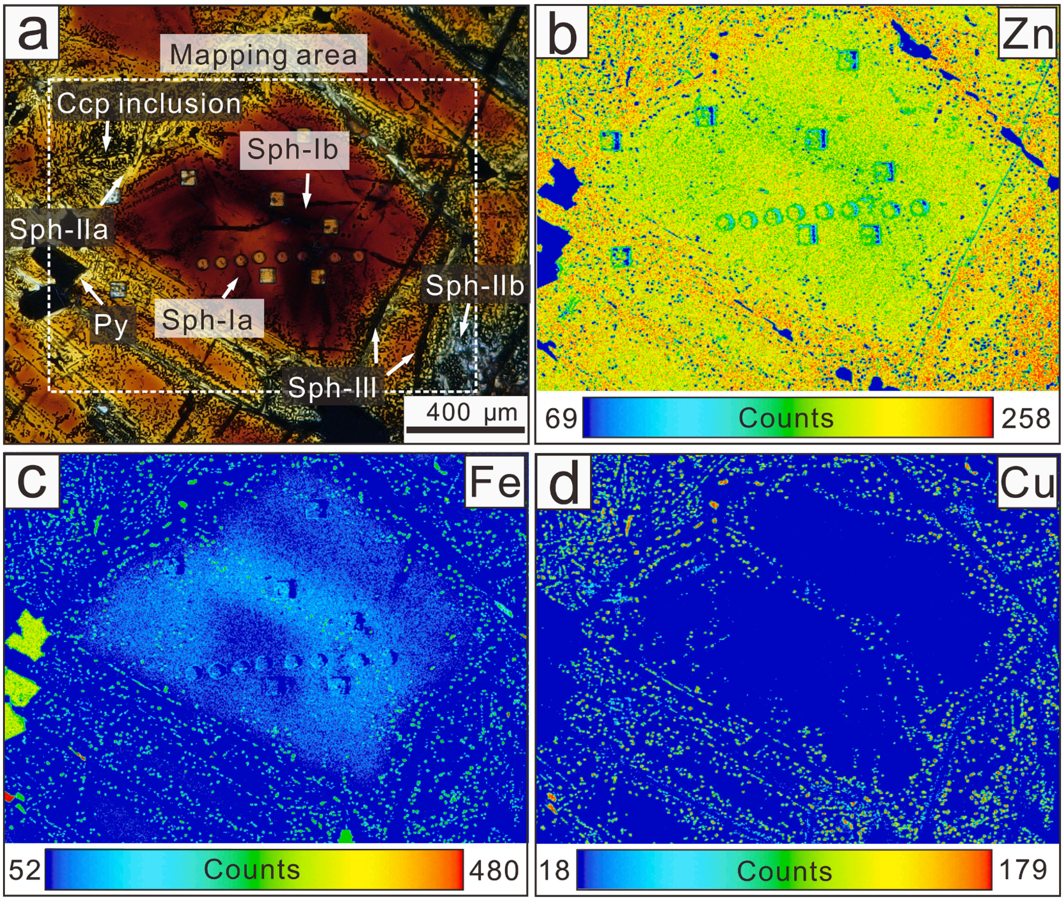

Fig. 8. Photomicrographs (transmitted light) and EPMA element maps of different generations of sphalerite. Note that the round and square spots are LA-(MC)ICP-MS spots.

estimated temperatures (Frenzel et al., 2016; 2022) and FeS contents in sphalerite (Table ESM1), the sulfur fugacity is calculated. The results revealed that Sph-Ia has the mean sulfur fugacity ($\log_{10}fS_2$) of −9.03 ± 0.03 and Sph-Ib of −8.26 ± 0.06. In contrast, Sph-IIa and Sph-IIb have a decreasing sulfur fugacity with $\log_{10}fS_2$ values of −10.63 ± 0.19 and −11.77 ± 0.38, respectively. Sph-III gives mean $\log_{10}fS_2$ values of −10.82 ± 0.29 (Table 1).

5.3. *Element distribution in sphalerite*

In EPMA maps, the areas with higher Fe and Cu contents are characterized by relatively lower Zn content (Fig. 8b-d). Fe and Cu element maps display chalcopyrite inclusions with the most widespread in Sph-IIa and subordinate in Sph-Ib (Fig. 8c, d). After excluding the element anomalies from mineral inclusions, Sph-Ib has the highest Fe contents in all the sphalerite varieties, while Fe tends evenly distributed within Sph-Ia (Fig. 8c).

LA-ICP-MS trace element maps (Fig. 9) reveal composite sphalerite consisting of oscillatory-zoned Sph-I in the core, Sph-IIa in the rim and Sph-III veinlets. The dark Sph-Ib bands generally have high Fe, Cd, Mn, Cu, Ag and In but relatively low Zn concentrations (Fig. 9b-i). Specifically, the Fe-, Mn- and Cd-rich zones are mainly overlapped in Sph-Ib (Fig. 9c-e), while the Cu- and Ag-rich zones are generally consistent (Fig. 9g, h) but antithetical to the zoning patterns of Fe, Mn and Cd. The In map displays the best-developed rhythmic zoning, which overlaps with Cu- and Ag-rich zones in Sph-I (Fig. 9g-i). In contrast, Ga has a distinct distribution pattern in the element maps, i.e., local sector zoning. Sph-IIa and Sph-III have different element distribution patterns from Sph-I. Particularly, Sph-IIa is characterized by higher contents of Zn, Cu and Ag (Fig. 9b, g, h), and Sph-III is higher in Cu and Ag compared to Sph-I (Fig. 9g, h).

5.4. *Principal component analysis*

In the PCA loading biplot (Fig. 10), the arrow angles of two elements are determined by the covariance of element concentration (Bauer et al., 2019), and thus indicate the correlation of elements as well as similarities of geochemical behavior. The PCA results based on the log-transformed trace element concentration dataset yield a total variance of 72.3% explained by the first principal component (PC1, 55.1%) and the second principal component (PC2, 17.2%) for Sph-I (Fig. 10b). Manganese, Fe, Cu, Ag, Cd, In and Sn are mainly measured by PC1 to PC4. The scoring and loading biplot demonstrate that the data points of Sph-Ia and Sph-Ib are separate into two clusters (Fig. 10a, c), and two distinct element groups were identified: group-1 is composed of Ag, Cu and In, group-2 comprises Fe, Mn, Cd and Sn.

Principal components of PC1 (37.1%) and PC2 (23.2%) account for 60.3% of the total variance of Sph-II (Fig. 10e). The Sph-IIa and Sph-IIb populations appear to divide into two distinct clusters, showing minimal overlap (Fig. 10d). Based on the element correlation, three groups of elements are observed (Fig. 10d): Fe + Mn, Ag + Cu + Sn + Cd and In. As for Sph-III, PC1 (51.8%) and PC2 (18.2%) have a combined variance of 70% (Fig. 10h), and three major element groups are identified: Fe + Mn (group-1), Cu + Ag + Cd + Sn (group-2) and In (group-3). In general, In exhibits distinct geochemical behavior as indicated by the negative or unrelated correlation with other elements in Sph-II and Sph-III. In contrast, Cu and Ag are highly correlated and described by the same principal component.

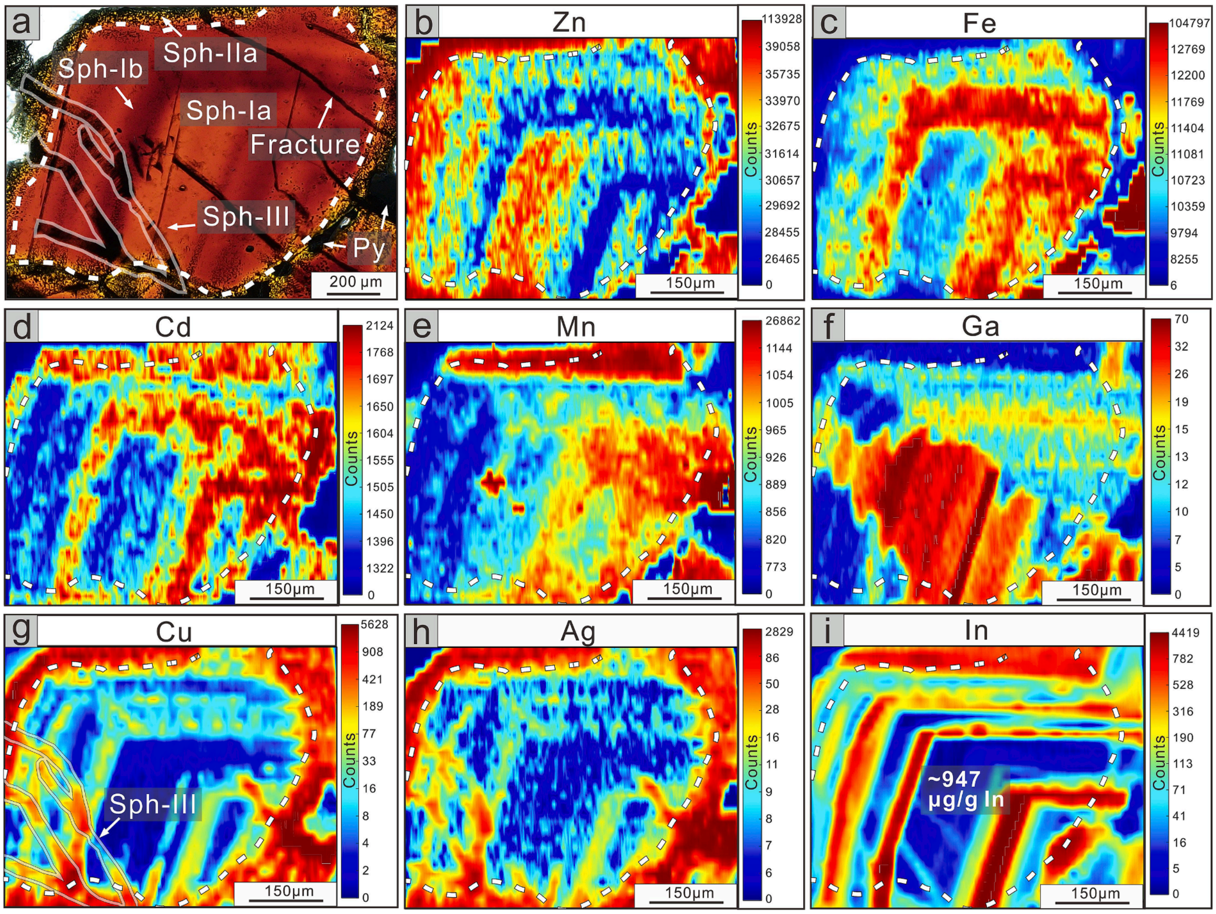

Fig. 9. Photomicrographs (transmitted light) and LA-ICP-MS trace element maps of sphalerite composite grain consisting of Sph-I, Sph-IIa and Sph-III. The boundary between Sph-I and Sph-IIa is marked by white dashed line, while gray solid lines delineate the Sph-III veinlets.

5.5. Sulfur isotopes

Sph-I has $\delta^{34}S_{\text{V-CDT}}$ values from −3.0 to −1.7‰ (n = 15), Sph-II has $\delta^{34}S_{\text{V-CDT}}$ values varying between −2.7 and −1.7‰ (n = 12), and Sph-III yields $\delta^{34}S_{\text{V-CDT}}$ values between −2.8 and −2.0‰ (n = 5), indicating a relatively uniform sulfur isotopic composition. In contrast, pyrite has a relatively large $\delta^{34}S_{\text{V-CDT}}$ variation ranging from −2.1 to 3.5‰ (n = 6) (Fig. 11 and Table ESM 6).

5.6. Muscovite ^{40}Ar/^{39}Ar geochronology

The corresponding plateau, isochron and inverse isochron age diagrams are presented in Fig. 12. The ^{40}Ar/^{39}Ar data exhibited a flat distribution in plateaus indicating no disturbance by late thermal events. The plateau date in the range of 4.8% to 30% laser energy is ca. 121.4 ± 1.2 Ma (MSWD = 0.52, Fig. 12b), which accounts for 85.09% of the total ^{39}Ar released. The corresponding isochron date is ca. 121.8 ± 1.2 Ma (MSWD = 0.54, Fig. 12b) and the inverse isochron date is ca. 121.7 ± 1.2 Ma (MSWD = 0.52, Fig. 12d). The initial ^{40}Ar/^{36}Ar ratios of 282.2 ± 8.5 and 283.8 ± 8.5 for the isochron and inverse isochron plots are close to the atmospheric value (295.5; Marty et al., 1989; Burnard et al., 1999). The plateau date is in good agreement with the isochron and inverse isochron dates, indicating that hydrothermal muscovite alteration occurs at ca. 121.1 ± 2 Ma.

6. Discussion

6.1. Element distribution and substitution mechanism

Micro-scale inclusions are often identified as peaks in LA-ICP-MS ablation profiles, and conversely, flat signal spectra indicate that elements are present in solid solution or evenly distributed nano-particles (Cook et al., 2009; Ye et al., 2011). Generally, time-resolved depth profiles of the Jingchong sphalerite exhibit smooth signal patterns of Mn, Co, Ni, Ga, Ge and Cd (Fig. 13). Most Fe and Cu profiles exhibit relatively flat features for all sphalerite varieties, indicating they are mainly present as solid solutions. However, a few peaks of Fe and Cu signals are observed in Sph-Ib and Sph-IIa ablation profiles (Fig. 13b, c). Their compatible trends further imply that these anomalous peaks are caused by chalcopyrite inclusions. This is consistent with bleb-shaped anomalies in EMPA maps (Fig. 8a, c, d). In addition, some Fe peaks unparallel with Cu signals in Sph-I profiles may be attributed to the presence of pyrite and/or pyrrhotite inclusions (Fig. 5e). Besides, the spiky spectra of Ag, In and Sn in Sph-IIa and Sph-III presented similar trends which are compatible to Fe and Cu signals (Fig. 13c, e), indicating that Ag, In and Sn occur in both solid solution and chalcopyrite inclusions. Noticeably, only the smooth signal sections in the time-resolved depth profiles were selected for data processing, i.e., the interference of micro-scale mineral inclusions on the trace element compositions of sphalerite are negligible.

Divalent cations such as Fe, Mn, Cd and Co commonly substitute Zn^{2+} directly, while monovalent cations like Cu^{+} and Ag^{+} are favored to be incorporated into sphalerite lattice by coupled substitution with trivalent and/or tetravalent cations such as In^{3+}, Ga^{3+}, Sn^{3+}, Sn^{4+} and

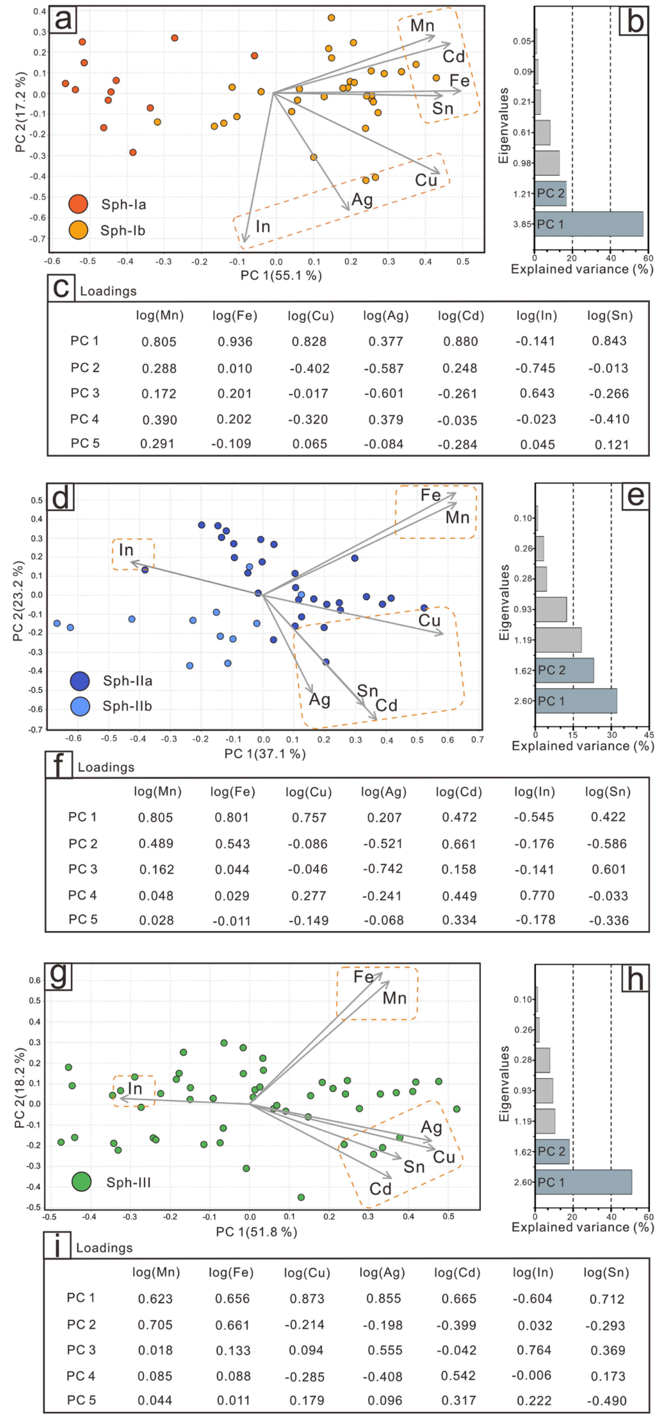

c Loadings

	log(Mn)	log(Fe)	log(Cu)	log(Ag)	log(Cd)	log(In)	log(Sn)
PC 1	0.805	0.936	0.828	0.377	0.880	-0.141	0.843
PC 2	0.288	0.010	-0.402	-0.587	0.248	-0.745	-0.013
PC 3	0.172	0.201	-0.017	-0.601	-0.261	0.643	-0.266
PC 4	0.390	0.202	-0.320	0.379	-0.035	-0.023	-0.410
PC 5	0.291	-0.109	0.065	-0.084	-0.284	0.045	0.121

f Loadings

	log(Mn)	log(Fe)	log(Cu)	log(Ag)	log(Cd)	log(In)	log(Sn)
PC 1	0.805	0.801	0.757	0.207	0.472	-0.545	0.422
PC 2	0.489	0.543	-0.086	-0.521	0.661	-0.176	-0.586
PC 3	0.162	0.044	-0.046	-0.742	0.158	-0.141	0.601
PC 4	0.048	0.029	0.277	-0.241	0.449	0.770	-0.033
PC 5	0.028	-0.011	-0.149	-0.068	0.334	-0.178	-0.336

i Loadings

	log(Mn)	log(Fe)	log(Cu)	log(Ag)	log(Cd)	log(In)	log(Sn)
PC 1	0.623	0.656	0.873	0.855	0.665	-0.604	0.712
PC 2	0.705	0.661	-0.214	-0.198	-0.399	0.032	-0.293
PC 3	0.018	0.133	0.094	0.555	-0.042	0.764	0.369
PC 4	0.085	0.088	-0.285	-0.408	0.542	-0.006	0.173
PC 5	0.044	0.011	0.179	0.096	0.317	0.222	-0.490

Fig. 10. PCA plots of sphalerite chemical data. **a, d, g** A comprehensive score and loading plot showing clusters of elements with similar behavior. **b, e, h** Scree plot of the eigenvalues of the correlation matrix, explaining the variance. **c, f, i** Loadings of different elements for each principal component.

Ge^{4+} (Moh and Jager, 1978; Johan, 1988; Lepetit et al., 2003; Seifert and Sandmann, 2006; Cook et al., 2009, 2011; Bauer et al., 2019). Sphalerite in the Jingchong deposit displays complicated textural and chemical patterns (Figs. 8–9), indicating distinct substitution mechanisms among the different generations. The LA-ICP-MS mapping identified the element groups of Fe + Cd + Mn and Cu + Ag + In based on their distinct zoning patterns (Fig. 9). In conjunction with the negative correlations between Zn and Fe + Mn + Cd + Sn (Fig. 7a), as well as the intimate relations of Fe + Mn + Cd + Sn in PCA (Fig. 10a), the following direct substitutions are proposed in Sph-I: $Zn^{2+} \leftrightarrow (Fe, Mn, Cd, Sn)^{2+}$. Given that Fe^{3+} commonly exists in Fe-rich sphalerite with more than 10 mol.% FeS at high sulfur fugacity (Lepetit et al., 2003), the incorporation of Fe^{3+} in the Jingchong sphalerite was not considered. In Sph-I, a coupled substitution of $2Zn^{2+} \leftrightarrow (Cu, Ag)^{+} + In^{3+}$ is proposed based on the relatively narrow angles between In, Cu and Ag in the PCA biplot and the positive correlation of Cu + Ag and In in Fig. 7b. Besides, the positive correlations in Cu + Ag vs. In + Sn, Cu + Ag vs. Sn and In vs. Sn plots (Fig. 7c-e) show that the data points are generally distributed along the lines of (Cu + Ag)/(In + Sn) = 1:1, (Cu + Ag)/(Sn) = 1:1 and 2:1, In/Sn = 1:1. These observations suggest the coupled substitution of $4Zn^{2+} \leftrightarrow \mathbf{2}\,(Cu, Ag)^{+} + Sn^{3+} + In^{3+}$, $2Zn^{2+} \leftrightarrow (Cu, Ag)^{+} + Sn^{3+}$, $3Zn^{2+} \leftrightarrow 2(Cu, Ag)^{+} + Sn^{4+}$ and $3Zn^{2+} \leftrightarrow Sn^{3+} + In^{3+} + \square$ (vacancy) may exist in Sph-I at Jingchong.

Different from Sph-I, PCA reveals different groups of Fe + Mn, Cu + Ag + Cd + Sn and In in Sph-II and Sph-III. This is consistent with the results that Sph-II and Sph-III generally show higher Cd, Cu, Ag, Ga and Ge but lower Fe and Mn contents with variable In concentration compared to Sph-I (Figs. 6, 10). Thus, the following direct substitution may be incorporated into Sph-II and Sph-III: $Zn^{2+} \leftrightarrow (Fe, Mn)^{2+}$. Besides, the weak negative correlation between Fe and Cd in PCA plots and their opposite distribution patterns in Sph-II and Sph-III (Fig. 9c, d and Fig. 10d, g) indicate that there is elemental competition between Fe and Cd, which can be described as $Fe^{2+} \leftrightarrow Cd^{2+}$. Notably, In tends to decouple from Cu and Ag in Sph-II and Sph-III (Fig. 9g-i) and exhibits uncorrelated or negative correlations with Cu, Ag and Fe in PCA (Fig. 10d, g). This is further confirmed by the irrelevance of Cu + Ag and In and the weak negative correlation between Fe and In as shown in Fig. 7b and f. These findings contradict many previous research studies in which In is commonly coupled with Cu and Ag and incorporated into sphalerite as solid solution or mineral inclusions, e.g., chalcopyrite ($CuFeS_2$), stannite (Cu_2FeSnS_4), roquesite ($CuInS_2$) and sakuraiite ($CuZn_2InS_4$) (Cook et al., 2009; Pavlova et al., 2015; Bauer et al., 2017; Xu et al., 2020). Here, we infer that the following substitution could also exist in Sph-II and Sph-III: $3(Zn, Fe)^{2+} \leftrightarrow 2In^{3+} + \square$ (vacancy).

6.2. *Sphalerite formation mechanism*

Oscillatory zoning as a common texture could be caused either by fluctuations of the physicochemical conditions under open systems or by the internal diffusion-limited self-organization process in closed systems (Reeder et al., 1990; Shore and Fowler, 1996; Holten et al., 1997; L'Heureux and Jamtveit, 2002; Di Benedetto, 2005). In the Jingchong deposit, no significant variations of the physicochemical conditions between Sph-Ia and Sph-Ib bands (Fig. 14) preclude the external mechanism caused by environmental fluctuations. Instead, the alternated Fe + Cd + Mn-rich and Cu + Ag + In-rich zones in Sph-I (Fig. 9) reveal the competition among these elements for incorporation into the crystal structure. Such element competition mechanisms are referred as self-organized non-equilibrium processes during crystal growth (Pattrick et al., 1993; L'Heureux, 2000, 2013; Katsev and L'Heureux, 2001; Di Benedetto, 2005). The presence of sector zoning of Ga in Sph-I (Fig. 9f) which implies the slow crystallization growth, further supports a kinetically-induced process (Watson and Liang, 1995). Therefore, the self-organized mechanism is a possible explanation for the formation of Sph-I and its oscillatory and sector zoning patterns.

The intimate intergrowth of sphalerite with pyrite, pyrrhotite and chalcopyrite has been interpreted as the products of exsolution, epitaxial growth, co-precipitation, or replacement (Wiggins and Craig, 1980). As for pyrite and pyrrhotite inclusions, they appear as oriented rows of blebs, ellipsoids or lamella, and are distributed discretely within Sph-I grains (Fig. 5e). This seems to preclude the likelihood of replacement (Wiggins and Craig, 1980), and instead exsolution formed the lamellar and ellipsoid intergrowths given the high Fe contents in Sph-I. It is supported by the partial overlap of the Sph-I ranges with the mineral reaction line of pyrite and pyrrhotite in Fig. 14 at relatively high

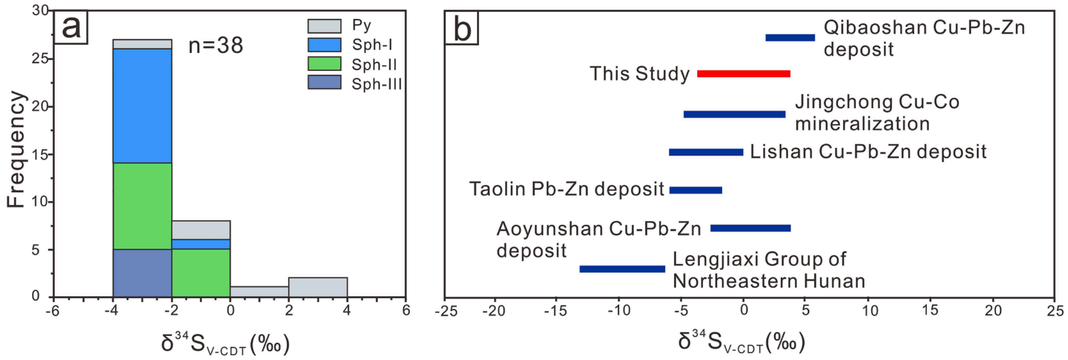

Fig. 11. **a** Histogram of sulfur isotopes of sphalerite and pyrite. b Comparison of sulfur isotope compositions from this study with those of the Neoproterozoic Lengjiaxi Group and the representative Pb-Zn deposits in northeastern Hunan Province. The $\delta^{34}S_{V\text{-}CDT}$ values of the Qibaoshan and Aoyunshan Cu-Pb-Zn deposits are from Liu et al. (2001), the Jingchong Cu-Co ores from Wang et al. (2017, 2022), the Lishan Cu-Pb-Zn deposit from Yu et al. (2021), and the Lengjiaxi Group from Luo (1990) and Liu et al. (1999).

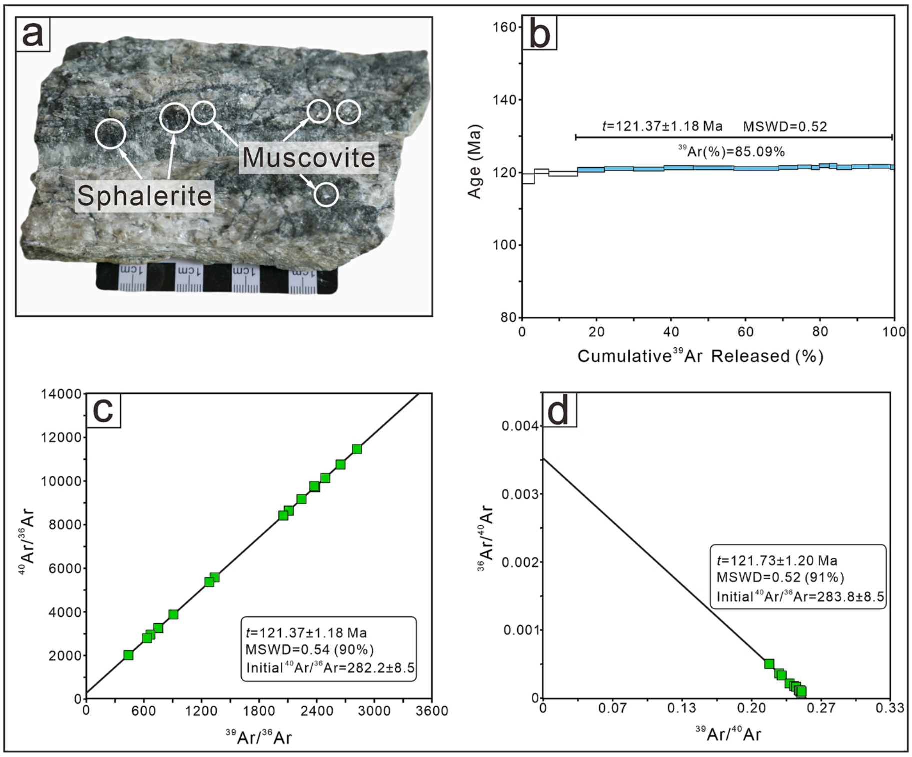

Fig. 12. The altered rock sample **(a)** and the ^{40}Ar-^{39}Ar plateau age **(b)**, isochron age **(c)** and inverse isochron age **(d)** of muscovite in the Jingchong deposit.

temperature and sulfur fugacity conditions. The separation of pyrite and pyrrhotite inclusions most likely occurred from the Fe-rich ZnS metastable solid solution due to cooling or decompression (Wiggins and Craig, 1980; Bortnikov et al., 1991; Einaudi et al., 2003). However, exsolution is not an alternative formation mechanism for chalcopyrite inclusions due to the limited Cu-solubility in sphalerite (Kojima and Sugaki, 1985; Sugaki et al., 1987; Barton and Bethke, 1987; Kojima, 1990; Cook et al., 2009; Govindarao et al., 2018). The relatively high Fe contents in the dark Sph-Ib bands (av. 9.24 wt%), combined with the abundance of coexisting chalcopyrite inclusions, verified the potential of local supersaturation of Fe^{2+} and Cu^{+} at the mineral-fluid interfaces. Consequently, chalcopyrite inclusions parallel to the growth zones of Sph-I are most likely formed by co-precipitation (Mizukami and Ohmori 1989; Kojima 1990; Bortnikov et al., 1991; Kojima et al., 1995).

Sph-IIa occurs along fractures or grain boundaries of Sph-I (Figs. 5a, b, c, h and 8a). The sharp contact (Fig. 5b, c) and remarkable changes in chemical compositions (such as Zn, Fe, Cd, Cu and Ag) between Sph-I and Sph-IIa (Figs. 6–8) indicate that Sph-IIa most likely formed by fluid-mediated coupled dissolution-reprecipitation reaction (CDR) (Altree-Williams et al., 2015). The fractures and grain boundaries of Sph-I can serve as the significant fluid pathway to the CDR reactions (Røyne et al., 2008; Jamtveit et al., 2009) and therefore formed “core (Sph-I)-rim (Sph-IIa)” texture. The higher Cu contents and more chalcopyrite inclusions in Sph-IIa further suggest the fluid is elevated in Cu contents. Thus, the replacement of Sph-I by Sph-IIa is explained by the following reaction: $2Zn_{0.90}Fe_{0.10}S + 0.10Cu^{+} + 0.10H^{+} \rightarrow 1.80Zn_{0.95}Fe_{0.05}S + 0.10CuFeS_2 + 0.10Zn^{2+} + 0.05H_2$ (modified from Barton and Bethke, 1987, Eldridge et al., 1988, Bortnikov et al., 1991). During this reaction, the dissolution of Fe-rich Sph-I provides abundant Zn^{2+}, Fe^{2+} and S^{2-}, while fluids provide Cu^{+} and H^{+}, which caused the subsequent precipitation of Sph-IIa and chalcopyrite inclusions. According to the GGIMFis geothermometer, Sph-II was formed at the lower temperature and sulfur fugacity conditions relative to Sph-I (Fig. 14). This indicates that the influx of the low-T, -pH and -fS_2 fluid with

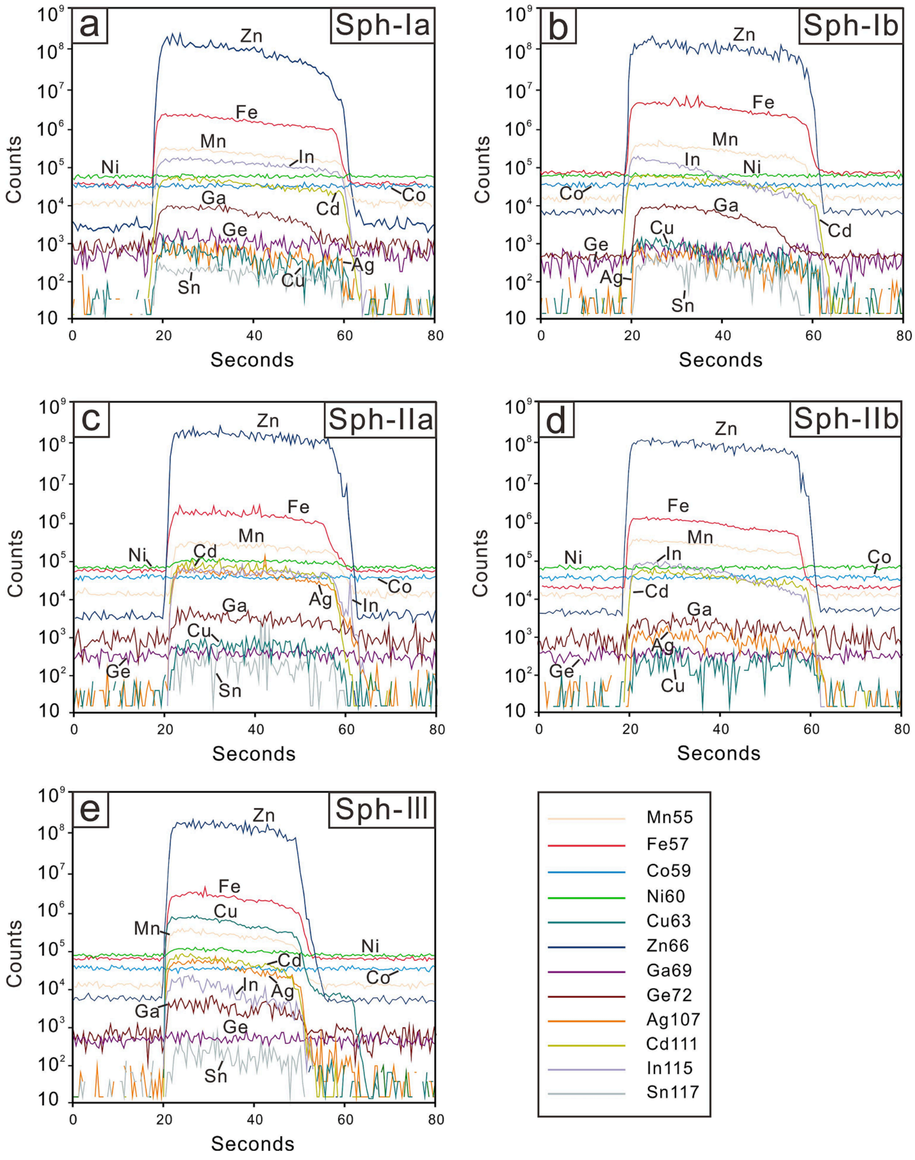

Fig. 13. Representative time-resolved depth profiles for selected elements from different sphalerite species.

elevated Cu level significantly facilitated the formation of Sph-IIa. After the extensive precipitation of Sph-IIa and chalcopyrite inclusions, the remaining fluids are depleted in Cu^+ and Fe^{2+}, and thus formed the Fe-poor Sph-IIb (rare chalcopyrite inclusions) with typical epitaxial texture. Relative to the formation temperature of 289 ± 55 °C for Sph-IIa, Sph-IIb yielded a lower temperature of 254 ± 60 °C, indicating Sph-IIb formed under decreasing temperature (Table 1; Fig. 14).

Sph-III is characterized by the “dusting“ or “watermelon”-like chalcopyrite inclusions with uneven sizes and distribution patterns (Fig. 5h, i), which are commonly regarded as the products of the solid-state diffusion mechanism (Bente and Doering, 1995; Blesgen et al., 2002, 2004, Blesgen, 2005; Bauer et al., 2017, 2019; Kaur et al., 2020). However, in our case, distinct textural and compositional boundaries between Sph-III and Sph-I/ Sph-II (Figs. 5a, b, h and 8), and the absence of massive Cu-sulfide sources preclude solid-state diffusion. Instead, it favors the formation mechanism of CDR (Putnis, 2009, 2018; Zhao et al., 2013; Altree-Williams et al., 2015). The dissolution of Sph-I, Sph-II and their mineral inclusions can provide abundant Zn^{2+}, Fe^{2+} and Cu^+ to form chalcopyrite inclusion-rich Sph-III. Nevertheless, given that the chalcopyrite inclusion is more abundant in Sph-III than Sph-I and Sph-II, a fluid pulse with elevated Cu contents may be involved during the Sph-III formation. Finally, a genetic model is built for the evolution of sphalerite varieties during Pb–Zn mineralization in the Jingchong deposit (Fig. 15).

6.3. *Correlation of Pb-Zn with Cu-Co mineralization*

The ^{40}Ar-^{39}Ar dating of muscovite from the hydrothermal alteration zone gives a plateau age of ca. 121.1 ± 2 Ma (Fig. 12). According to the presence of sphalerite in the altered rock sample, the plateau age could be regarded as the mineralizing time of the Jingchong Cu-Co-Pb-Zn deposit given that the hydrothermal system is not extremely long-lived. The obtained mineralizing age is consistent either with that of the Hengdong Co deposit (ca. 125 Ma, muscovite ^{40}Ar-^{39}Ar method; Zou et al., 2018) or the Taolin Pb-Zn deposit (ca. 121 Ma, muscovite ^{40}Ar-^{39}Ar method; Xu et al., 2022) within error and slightly younger than that of the Lishan Cu-Pb-Zn deposit (ca. 129 Ma, muscovite ^{40}Ar-^{39}Ar method; Xu et al., 2022). These geochronological data indicate that the Early Cretaceous (ca. 130–120 Ma) is an important Cu-Co-Pb-Zn mineralization period in the northeastern Hunan Province.

The abundance of trace elements such as Fe, Mn, Cu, Ga, Ge, Cd, In and Sn in sphalerite can serve as important indicators for its origin (Cook

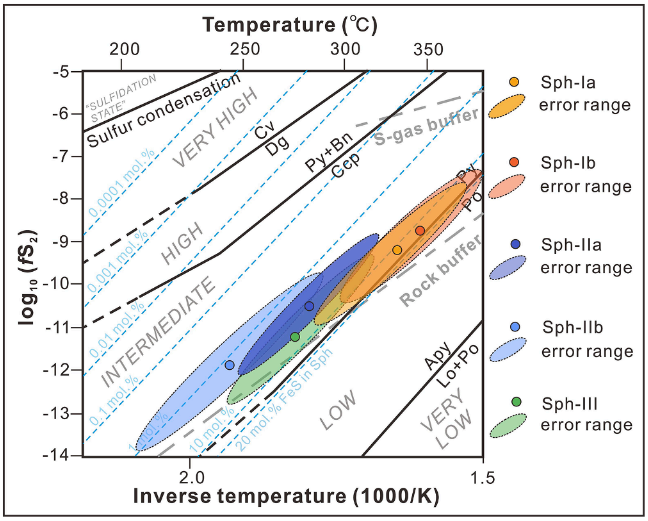

Fig. 14. Sulfur fugacity-inverse temperature plot (adapted from Einaudi et al., 2003; Frenzel et al., 2022) showing the location of different sphalerite species in the Jingchong deposit relative to mineral reaction lines (in black), the S-gas and rock buffers (in grey), and isolines (in blue) describing the variation in sphalerite Fe contents. Ellipses delineating the fields for sphalerite varieties correspond to 95% confidence intervals. Mineral abbreviations: Cv, covellite; Dg, digenite; Py, pyrite; Bn, bornite; Ccp, chalcopyrite; Po, pyrrhotite; Apy, arsenopyrite; Lo, löllingite.

et al., 2009; Ye et al., 2011; Belissont, 2014; Yu et al., 2020; Zhao et al., 2023). Generally, magmatic-hydrothermal sphalerite has higher Fe, Mn, Cu, In and Sn compared to those of non-magmatic-hydrothermal sphalerite (Canet et al., 2009; Murakami and Ishihara, 2013; Belissont, 2014; Bauer et al., 2019; Zhao et al., 2023). The Jingchong sphalerite exhibits Fe (av. 5.87 wt%), Mn (av. 229 ppm), Cu (av. 692 ppm), In (av. 46.5 ppm) and Sn (av. 44.0 ppm) concentrations, which are obviously higher than those in the non-magmatic-hydrothermal deposits (e.g., MVT, Jingding, Irish-type Pb-Zn deposits with generally Fe < 2 wt%, Mn < 100 ppm, Cu < 200 ppm, In < 1 ppm and Sn < 1 ppm; Ye et al., 2011; Bonnet et al., 2016; Zhou et al., 2018; Li et al., 2020; Yu et al., 2020; Song et al., 2020; Doran et al., 2022). Besides, the Cd/Fe and Cd/Mn ratios of the Jingchong sphalerite range from 0.013 to 0.054 and 1.21 to 4.12, respectively, consistent with that of magmatic-hydrothermal origin (Cd/Fe < 0.1, Cd/Mn < 5; Zhao et al., 2007; Cao et al., 2014; Yu et al., 2020).

In general, the measured $\delta^{34}S_{\text{V-CDT}}$ values of sulfide minerals are regarded as equivalent to those of fluids at low oxygen fugacity and pH conditions (Ohmoto and Goldhaber, 1997). Given the absence of sulfate minerals and Fe-oxides in the Pb-Zn mineral paragenesis and the medium–low formation temperature for different sphalerite types (Fig. 14), the measured $\delta^{34}S_{\text{V-CDT}}$ values can represent the sulfur isotopic composition of the ore-forming fluid. By comparison, the measured $\delta^{34}S_{\text{V-CDT}}$ values are obviously distinct from that of the Neoproterozoic Lengjiaxi Group (Fig. 11; Luo, 1990; Liu et al., 1994; Liu et al., 1999), indicating a non-strata sulfur origin. Instead, they are similar to those for the magmatic-hydrothermal vein-type Lishan (−5.1 to −0.4‰, Yu et al., 2021) and Taolin (−6.0 to −2.3‰, Yu et al., 2020) Pb-Zn (-Cu) deposits, and the skarn-porphyry Qibaoshan (+0.6 to +5.4‰; Liu et al., 2001) and Aoyushan (−2.9 to +3.3‰, Liu et al., 2001) Cu-Pb-Zn deposits in the northeastern Hunan Province. What is more, the measured $\delta^{34}S_{\text{V-CDT}}$ values (−2.79‰ to +3.47‰) of sulfides from Pb-Zn ores fall in the $\delta^{34}S_{\text{V-CDT}}$ range of Jingchong Co-Cu ores (−4.90‰ to +3.57‰, Wang et al., 2017, 2022), indicating a similar sulfur source for both Cu-Co- and Pb-Zn mineralization. Consequently, consistent with the Cu-Co ores (Wang et al., 2022), the Jingchong Pb-Zn ores most likely have a sulfur source predominantly from a magmatic reservoir (0 ± 5‰; Ohmoto and Rye, 1979).

The fluid cooling, boiling and mixing are considered as important metal precipitation mechanisms (Hemley et al., 1992; Hemley and Hunt, 1992). In the Jingchong deposit, no evidence supports that fluid boiling controlled Cu-Co-Pb-Zn deposition according to the available mineralogical and fluid inclusion data (Zhou and Kang, 2017). The integrated

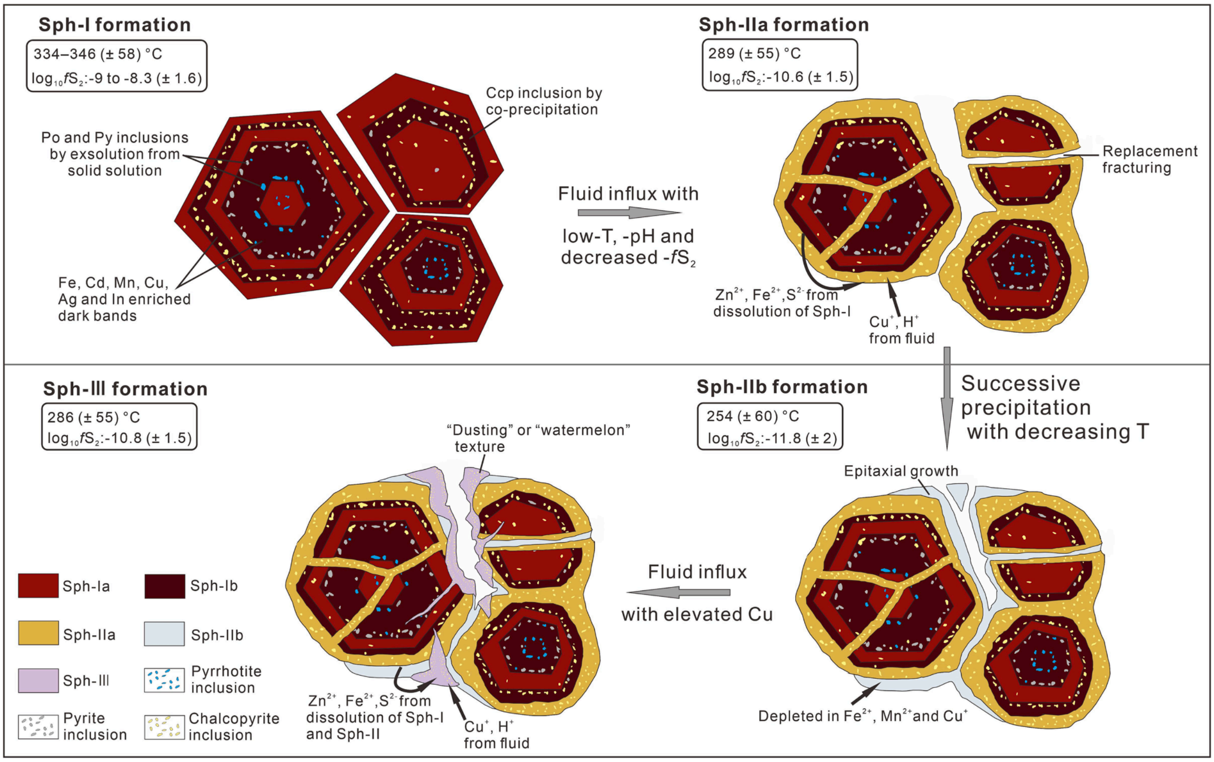

Fig. 15. Schematic diagram for the formation of three sphalerite generations in the Jingchong deposit.

mineralogical and sulfur isotope evidence have disclosed that the Jingchong Pb-Zn- and Cu-Co mineralization were formed in a magmatic-hydrothermal system with similar wall rock alteration. The He-Ar isotopes of Cu-Co ores revealed that the mixing of magmatic-hydrothermal fluids with meteoric water was a possible mechanism for metal precipitation (Wang et al., 2017, 2022). In combination with the consistent ore-forming temperature between the Cu-Co stages (256–318 °C, chlorite geothermometry; Wang et al., 2017) and Pb-Zn stage (286–346 °C, sphalerite geothermometry; this study), the mixing process is assumed to dominate the mineralization of Pb-Zn. The placement of Pb-Zn orebodies at the upward zoning of Cu-Co orebodies and the sequent precipitation of Pb-Zn following Cu-Co might be related to the mobility of these metals in hydrothermal fluids (Brugger et al., 2016). According to Soft-Hard Acid-Base theory (Pearson, 1963), chloride complexes are assumed to be the dominant Co, Cu, Pb and Zn species in hydrothermal solutions with the temperature of no more than 400 °C, and their stability is dependent not only on the temperature, salinity, pH and redox of ore-forming fluid but also the coordination chemistry of metals (Migdisov et al., 2011; Zhong et al., 2015; Brugger et al., 2016). As mentioned above, the varying physicochemical conditions are hardly considered as the main factors controlling the discrepant precipitation between Pb-Zn- and Cu-Co metals. Instead, the higher solubility of Pb and Zn complexes relative to Cu complex in hydrothermal fluids could explain the long-distance transportation of Pb-Zn than Cu (Hemley et al., 1992; Emsbo, 2000).

7. Conclusions

(1) Three generations of sphalerite are identified. Sph-I is featured by the oscillatory zones of Fe-, Cd- and Mn-rich alternating with Cu-, Ag- and In-rich and Ga sector zones. Sph-II and Sph-III have homogeneous but higher Cd, Cu and Ag concentrations compared to Sph-I. The following substitutions are identified in sphalerite species: $\mathrm{Zn}^{2+} \leftrightarrow (\mathrm{Fe, Mn, Cd, Sn})^{2+}$, $\mathrm{Fe}^{2+} \leftrightarrow \mathrm{Cd}^{2+}$, $2\mathrm{Zn}^{2+} \leftrightarrow (\mathrm{Cu, Ag})^{+} + \mathrm{In}^{3+}$, $4\mathrm{Zn}^{2+} \leftrightarrow 2(\mathrm{Cu, Ag})^{+} + \mathrm{Sn}^{3+} + \mathrm{In}^{3+}$, $2\mathrm{Zn}^{2+} \leftrightarrow (\mathrm{Cu, Ag})^{+} + \mathrm{Sn}^{3+}$, $3\mathrm{Zn}^{2+} \leftrightarrow 2(\mathrm{Cu, Ag})^{+} + \mathrm{Sn}^{4+}$, $3\mathrm{Zn}^{2+} \leftrightarrow \mathrm{Sn}^{3+} + \mathrm{In}^{3+} + \square$ (vacancy) and $3(\mathrm{Zn, Fe})^{2+} \leftrightarrow 2\mathrm{In}^{3+} + \square$ (vacancy).

(2) The sphalerite geothermometer gives average temperatures of 334 ± 56 °C for Sph-Ia, 346 ± 58 °C for Sph-Ib, 289 ± 55 °C for Sph-IIa, 254 ± 60 °C for Sph-IIb, and 286 ± 55 °C for Sph-III. The estimated sulfur fugacity ($\log_{10}f\mathrm{S}_2$) is −9.03 ± 0.03 for Sph-Ia, −8.26 ± 0.06 for Sph-Ib, −10.63 ± 0.19 for Sph-IIa, −11.77 ± 0.38 for Sph-IIb, and −10.82 ± 0.29 for Sph-III, indicating the fluctuant ore-forming conditions.

(3) The oscillatory and sector zonings of Sph-I are formed by the self-organized mechanism. Pyrite and pyrrhotite inclusions in Sph-I are exsolved, while chalcopyrite inclusions are co-precipitated. The Sph-II and Sph-III species and associated mineral inclusions are interpreted to be formed by CDR reactions with the aid of the influx of relatively Cu-elevated fluids and subsequent direct precipitation.

(4) The Jingchong deposit was most likely formed at ca. 121.1 ± 2 Ma based on muscovite $^{40}\mathrm{Ar}/^{39}\mathrm{Ar}$ dating, which is in agreement with the ca. 130–120 Ma Pb-Zn mineralizing events in the northeastern Hunan Province. The sulfur isotopic values (−3.0 to +3.5‰) of the Pb-Zn ores plot within the range of Cu-Co ores, indicating a similar sulfur reservoir. Together with the trace element affinity of sphalerite with magmatic-hydrothermal origin, the Jingchong Pb-Zn and Cu-Co mineralization was formed in a magmatic-hydrothermal system.

Declaration of Competing Interest

The authors declare that they have no known competing financial interests or personal relationships that could have appeared to influence the work reported in this paper.

Data availability

I have shared my data in the appendix at the Attach File step

Acknowledgments

This research was financially co-supported by the National Natural Science Foundation of China (No. 42372106, 41672077), Hunan Provincial Natural Science Foundation of China (No. 2021JJ30817), Jiangxi Provincial Natural Science Foundation of China (No. 20224ACB203008) and China Scholarship Council (CSC). LA-ICPMS facility at LERA KIT is supported by DFG grant INST 121384/213-1 FUGG. The authors sincerely thank Kirsten Drüppel and Ziqi Hu for LA-ICP-MS technical support, and Diogo Ribeiro and Matteo Luca Deidda for helpful discussion. A particular thank is given to editors and two anonymous reviewers for constructive reviews.

Appendix A. Supplementary material

Supplementary data to this article can be found online at https://doi.org/10.1016/j.oregeorev.2023.105667.

References

Altree-Williams, A., Pring, A., Ngothai, Y., Brugger, J., 2015. Textural and compositional complexities resulting from coupled dissolution–reprecipitation reactions in geomaterials. Earth Sci. Rev. 150, 628–651. https://doi.org/10.1016/j.earscirev.2015.08.013.

Bao, Z., Chen, L., Zong, C., Yuan, H., Chen, K., Dai, M., 2017. Development of pressed sulfide powder tablets for in situ sulfur and lead isotope measurement using LA-MC-ICP-MS. Int. J. Mass Spectrom. 421, 255–262. https://doi.org/10.1016/j.ijms.2017.07.015.

Barton, P.B., Bethke, P.M., 1987. Chalcopyrite disease in sphalerite Pathology and epidemiology. Am. Mineral. 72 (5–6), 451–467.

Bauer, M.E., Seifert, T., Burisch, M., Krause, J., Richter, N., Gutzmer, J., 2017. Indium-bearing sulfides from the Hämmerlein skarn deposit, Erzgebirge, Germany: evidence for late-stage diffusion of indium into sphalerite. Miner. Deposita 54, 175–192. https://doi.org/10.1007/s00126-017-0773-1.

Bauer, M.E., Burisch, M., Ostendorf, J., Krause, J., Frenzel, M., Seifert, T., Gutzmer, J., 2019. Trace element geochemistry of sphalerite in contrasting hydrothermal fluid systems of the Freiberg district, Germany: insights from LA-ICP-MS analysis, near-infrared light microthermometry of sphalerite-hosted fluid inclusions, and sulfur isotope geochemistry. Miner. Deposita 54, 237–262. https://doi.org/10.1007/s00126-018-0850-0.

Belissont, R., 2014. LA-ICP-MS analyses of minor and trace elements and bulk Ge isotopes in zoned Ge-rich sphalerites from the Noailhac–Saint-Salvy deposit (France): Insights into incorporation mechanisms and ore deposition processes. Geochim. Cosmochim. Acta 126, 518–540. https://doi.org/10.1016/j.gca.2013.10.052.

Bente, K., Doering, T., 1995. Experimental studies on the solid-state diffusion of Cu+ In in ZnS and on “Disease”, DIS (Diffusion Induced Segregations), in sphalerite and their geological applications. Mineral. Petrol. 53 (4), 285–305.

Blesgen, T., 2005. Existence and uniqueness for a model describing chalcopyrite disease within sphalerite. Commun. Partial Differ. Equ. 29, 523–546. https://doi.org/10.1081/PDE-120030407.

Blesgen, T., Luckhaus, S., Bente, K., 2002. Modeling and numerical simulation of diffusion-induced segregation. Cryst. Res. Technol. 37, 570. https://doi.org/10.1002/1521-4079(200206)37:6<570::aid-crat570>3.0.co;2-u.

Blesgen, T., Luckhaus, S., Bente, K., 2004. Diffusion induced segregation in the case of the ternary system sphalerite, chalcopyrite and cubanite. Cryst. Res. Technol. 39, 969–979. https://doi.org/10.1002/crat.200410282.

Bonnet, J., Mosser-Ruck, R., Caumon, M.-C., Rouer, O., Andre-Mayer, A.-S., Cauzid, J., Peiffert, C., 2016. Trace element distribution (Cu, Ga, Ge, Cd, and Fe) in sphalerite: from the Tennessee MVT deposits, USA, by combined EMPA, LA-ICP-MS, Raman Spectroscopy, and Crystallography. Can. Mineral. 54, 1261–1284. https://doi.org/10.3749/canmin.1500104.

Bortnikov, N.S., Genkin, A.D., Dobrovol’skaya, M.G., Muravitskaya, G.N., Filimonova, A. A., 1991. The nature of chalcopyrite inclusions in sphalerite; exsolution, coprecipitation, or “disease”? Econ. Geol. 86, 1070–1082. https://doi.org/10.2113/gsecongeo.86.5.1070.

Brugger, J., Liu, W., Etschmann, B., Mei, Y., Sherman, D.M., Testemale, D., 2016. A review of the coordination chemistry of hydrothermal systems, or do coordination changes make ore deposits? Chem. Geol. 447, 219–253. https://doi.org/10.1016/j.chemgeo.2016.10.021.

Burnard, P.G., Hu, R., Turner, G., Bi, X.W., 1999. Mantle, crustal and atmospheric noble gases in Ailaoshan gold deposits, Yunnan Province, China. Geochim. Cosmochim. Acta 63, 1595–1604. https://doi.org/10.1016/S0016-7037(99)00108-8.

Canet, C., Camprubí, A., González-Partida, E., Linares, C., Alfonso, P., Piñeiro-Fernández, F., Prol-Ledesma, R.M., 2009. Mineral assemblages of the Francisco I.

Madero Zn-Cu-Pb-(Ag) deposit, Zacatecas, Mexico: implications for ore deposit genesis. Ore Geol. Rev. 35 (3–4), 423–435.

Cao, H.W., Zhang, S.T., Zheng, L., Liu, R.P., Tian, H.H., Zhang, X.H., Li, J.J., 2014. Geochemical characteristics of trace element of sphalerite in the Zhongyuku (Pb)-Zn deposit of the Luanchuan, southwest of China. J. Miner. Petrol. 34 (3), 50–59 (in Chinese with English abstract).

Charvet, J., Shu, L., Shi, Y., Guo, L., Faure, M., 1996. The building of South China: collision of Yangzi and Cathaysia blocks, problems and tentative answers. J. Asian Earth Sci. 13, 223–235.

Charvet, J., Shu, L., Faure, M., Choulet, F., Bo, W., Lu, H., Breton, N.L., 2010. Structural development of the lower Paleozoic belt of south China: genesis of an intracontinental orogen. J. Asian Earth Sci. 39, 309–330.

Chen, Y.C., 2014. Outline of regional metallogeny of ore deposits associated with the Mesozoic magmatism in South China. Geotecton. Metallog. 02, 219–229 (in Chinese).

ÇiFtçi̇, E., 2011. Sphalerite associated with pyrrhotite-chalcopyrite ore occurring in the Kotana Fe-Skarn deposit (Giresun, NE Turkey): exsolution or replacement. Turk. J. Earth Sci. 20, 307–320. https://doi.org/10.3906/yer-1001-26.

Cook, N.J., Ciobanu, C.L., Pring, A., Skinner, W., Shimizu, M., Danyushevsky, L., Saini-Eidukat, B., Melcher, F., 2009. Trace and minor elements in sphalerite: a LA-ICPMS study. Geochim. Cosmochim. Acta 73, 4761–4791. https://doi.org/10.1016/j.gca.2009.05.045.

Cook, N.J., Ciobanu, C.L., Danyushevsky, L.V., Gilbert, S., 2011. Minor and trace elements in bornite and associated Cu-(Fe)-sulfides: A LA-ICP-MS studyBornite mineral chemistry. Geochim. Cosmochim. Acta 75, 6473–6496. https://doi.org/10.1016/j.gca.2011.08.021.

Cugerone, A., Cenki-Tok, B., Muñoz, M., Kouzmanov, K., Oliot, E., Motto-Ros, V., Le Goff, E., 2020. Behavior of critical metals in metamorphosed Pb-Zn ore deposits: example from the Pyrenean Axial Zone. Miner. Deposita 56, 685–705. https://doi.org/10.1007/s00126-020-01000-9.

Deng, T., Xu, D., Chi, G., Wang, Z., Jiao, Q., Ning, J., Dong, G., Zou, F., 2017. Geology, geochronology, geochemistry and ore genesis of the Wangu gold deposit in northeastern Hunan Province, Jiangnan Orogen, South China. Ore Geol. Rev. 88, 619–637. https://doi.org/10.1016/j.oregeorev.2017.01.012.

Deng, T., Xu, D., Chi, G., Wang, Z., Chen, G., Zhou, Y., Li, Z., Ye, T., Yu, D., 2020. Caledonian (Early Paleozoic) veins overprinted by Yanshanian (Late Mesozoic) gold mineralization in the Jiangnan Orogen: A case study on gold deposits in northeastern Hunan, South China. Ore Geol. Rev. 124 https://doi.org/10.1016/j.oregeorev.2020.103586.

Di Benedetto, F., 2005. Compositional zoning in sphalerite crystals. Am. Mineral. 90, 1384–1392. https://doi.org/10.2138/am.2005.1754.

Doran, A.L., Hollis, S.P., Menuge, J.F., Piercey, S.J., Boyce, A.J., Johnson, S., Güven, J., Turner, O., 2022. A distal, high-grade Irish-type orebody: petrographic, sulfur isotope, and sulfide chemistry of the Island Pod Zn-Pb orebody, Lisheen, Ireland. Econ. Geol. 117, 305–326. https://doi.org/10.5382/econgeo.4882.

Einaudi, M.T., Hedenquist, J.W., Inan, E.E., 2003. Sulfidation state of hydrothermal fluids: the porphyry-epithermal transition and beyond. Soc. Econ. Geol. Spec. Publ. 10, 285–313.

Eldridge, C.S., Bourcier, W.L., Ohmoto, H., Barnes, H.L., 1988. Hydrothermal inoculation and incubation of the chalcopyrite disease in sphalerite. Econ. Geol. 83 (5), 978–989.

Emsbo, P., 2000. "Gold in Sedex deposits", Gold in 2000. In: Steffen G. Hagemann, Philip E. Brown. (Eds.), Society of Economic Geologists, pp. 427–437. https://doi.org/10.5382/Rev.13.13.

Frenzel, M., Hirsch, T., Gutzmer, J., 2016. Gallium, germanium, indium, and other trace and minor elements in sphalerite as a function of deposit type — A meta-analysis. Ore Geol. Rev. 76, 52–78. https://doi.org/10.1016/j.oregeorev.2015.12.017.

Frenzel, M., Voudouris, P., Cook, N.J., Ciobanu, C.L., Gilbert, S., Wade, B.P., 2022. Evolution of a hydrothermal ore-forming system recorded by sulfide mineral chemistry: a case study from the Plaka Pb-Zn-Ag Deposit, Lavrion, Greece. Miner. Deposita 57, 417–438. https://doi.org/10.1007/s00126-021-01067-y.

Fu, J., Hu, Z., Zhang, W., Yang, L., Liu, Y., Li, M., Zong, K., Gao, S., Hu, S., 2016. In situ sulfur isotopes (δ^{34}S and δ^{33}S) analyses in sulfides and elemental sulfur using high sensitivity cones combined with the addition of nitrogen by laser ablation MC-ICP-MS. Anal. Chim. Acta 911, 14–26. https://doi.org/10.1016/j.aca.2016.01.026.

Gao, L.Z., Chen, J., Ding, X.Z., Liu, Y.R., Zhang, C.H., Zhang, H., Liu, Y.X., Pang, W.H., Zhang, Y.H., 2011. Zircon SHRIMP U-Pb dating of the tuff bed of Lengjiaxi and Banxi groups, northeastern Hunan: constraints on the Wuling Movement. Geol. Bull. China 30 (07), 1001–1008 (in Chinese with English abstract).

George, L.L., Cook, N.J., Ciobanu, C.L., 2016. Partitioning of trace elements in co-crystallized sphalerite-galena-chalcopyrite hydrothermal ores. Ore Geol. Rev. 77, 97–116. https://doi.org/10.1016/j.oregeorev.2016.02.009.

Govindarao, B., Pruseth, K.L., Mishra, B., 2018. Sulfide partial melting and chalcopyrite disease: an experimental study. Am. Mineral. 103, 1200–1207. https://doi.org/10.2138/am-2018-6477.

Guo, F., Wang, Z.L., Xu, D.R., Dong, G.J., Ning, J.T., Wang, Z., Deng, T., Yu, D.S., Cui, Y., 2018. Genesis of the Lishan Pb-Zn-Cu polymetallic deposit in northeastern Hunan Province: evidences from the geology, mineralogy and sulfur isotopes. J. Nanjing Univ. (Nat Sci) 54 (2), 366–385 (in Chinese with English abstract).

Hemley, J.J., Cygan, G.L., Fein, J.B., Robinson, G.R., d'Angelo, W.M., 1992. Hydrothermal ore-forming processes in the light of studies in rock-buffered systems; I, Iron-copper-zinc-lead sulfide solubility relations. Econ. Geol. 87 (1), 1–22.

Hemley, J.J., Hunt, J.P., 1992. Hydrothermal ore-forming processes in the light of studies in rock-buffered systems; II, Some general geologic applications. Econ. Geol. 87 (1), 23–43.

Holten, T., Jamtveit, B., Meakin, P., Cortini, M., Blundy, J., Austrheim, H., 1997. Statistical characteristics and origin of oscillatory zoning in crystals. Am. Mineral. 82, 596–606. https://doi.org/10.2138/am-1997-5-619.

Hua, R., Chen, P., Zhang, W., Lu, J., 2005. Three large-scale metallogenic events related to the Yanshanian Period in Southern China. In: Mao, J., Bierlein, F.P. (Eds.), Mineral Deposit Research: Meeting the Global Challenge. Springer, Berlin Heidelberg, Berlin, Heidelberg, pp. 401–404. https://doi.org/10.1007/3-540-27946-6_105.

Jamtveit, B., Putnis, C.V., Malthe-Sørenssen, A., 2009. Reaction induced fracturing during replacement processes. Contrib. Miner. Petrol. 157, 127–133.

Ji, W., Lin, W., Faure, M., Chen, Y., Chu, Y., Xue, Z., 2017. Origin of the Late Jurassic to Early Cretaceous peraluminous granitoids in the northeastern Hunan Province (middle Yangtze region), South China: Geodynamic implications for the Paleo-Pacific subduction. J. Asian Earth Sci. 141, 174–193. https://doi.org/10.1016/j.jseaes.2016.07.005.

Jochum, K.P., Weis, U., Schwager, B., Stoll, B., Wilson, S.A., Haug, G.H., Andreae, M.O., Enzweiler, J., 2016. Reference values following ISO guidelines for frequently requested rock reference materials. Geostand. Geoanalytical Res. 40, 333–350. https://doi.org/10.1111/j.1751-908X.2015.00392.x.

Johan, Z., 1988. Indium and germanium in the structure of sphalerite: an example of coupled substitution with copper. Mineral. Petrol. 39, 211–229.

Katsev, S., L'Heureux, I., 2001. Two-dimensional model of banding pattern formation in minerals by means of coarsening waves: Mississippi Valley-type sphalerite. Phys. Lett. A 292, 66–74. https://doi.org/10.1016/S0375-9601(01)00767-8.

Kaur, N., Deng, C., Ojo, O.A., 2020. Effect of solute segregation on diffusion induced grain boundary migration studied by molecular dynamics simulations. Comput. Mater. Sci 179, 109685. https://doi.org/10.1016/j.commatsci.2020.109685.

Keith, M., Haase, K.M., Schwarz-Schampera, U., Klemd, R., Petersen, S., Bach, W., 2014. Effects of temperature, sulfur, and oxygen fugacity on the composition of sphalerite from submarine hydrothermal vents. Geology 42, 699–702. https://doi.org/10.1130/g35655.1.

Kojima, S., 1990. A coprecipitation experiment on intimate association of sphalerite and chalcopyrite and its bearings on the genesis of Kuroko ores. Mining. Geol. 40 (221), 147–158.

Kojima, S., Sugaki, A., 1987. An experimental study on chalcopyritization of sphalerite induced by hydrothermally metasomatic reactions. Mining. Geol. 37 (206), 373–380.

Kojima, S., Nagase, T., Inoue, T.A., 1995. Coprecipitation experiment on the chalcopyrite disease texture involving Fe-bearing sphalerite. J. Mineral. Petrol. Econ. Geol. 90, 261–267.

Kojima, S., Sugaki, A., 1985. Phase relations in the Cu-Fe-Zn-S system between 500 degrees and 300 degrees C under hydrothermal conditions. Econ. Geol. 80 (1), 158–171.

Koppers, A.A.P., 2002. ArArCALC—software for ^{40}Ar/^{39}Ar age calculations. Comput. Geosci. 28, 605–619. https://doi.org/10.1016/S0098-3004(01)00095-4.

L'Heureux, I., 2000. Origin of banded patterns in natural sphalerite. Phys. Rev. E 62, 3234–3245. https://doi.org/10.1103/PhysRevE.62.3234.

L'Heureux, I., 2013. Self-organized rhythmic patterns in geochemical systems. Philos. Trans. R. Soc. Math. Phys. Eng. Sci. 371, 20120356. https://doi.org/10.1098/rsta.2012.0356.

L'Heureux, I., Jamtveit, B., 2002. A model of oscillatory zoning in solid solutions grown from aqueous solutions: applications to the (Ba, Sr)SO_4 system. Geochim. Cosmochim. Acta 66, 417–429. https://doi.org/10.1016/S0016-7037(01)00792-X.

Lepetit, P., Bente, K., Doering, T., Luckhaus, S., 2003. Crystal chemistry of Fe-containing sphalerites. Phys. Chem. Miner. 30, 185–191. https://doi.org/10.1007/s00269-003-0306-6.

Li, X.H., 1999. U-Pb zircon ages of granites from the southern margin of the Yangtze Block: timing of Neoproterozoic Jinning Orogeny in SE China and implications for Rodinia assembly. Precambr. Res. 97, 43–57.

Li, X.H., 2000. Cretaceous magmatism and lithospheric extension in Southeast China. J. Asian Earth Sci. 18 (3), 293–305.

Li, Z., Ye, L., Hu, Y., Wei, C., Huang, Z., Yang, Y., Danyushevsky, L., 2020. Trace elements in sulfides from the Maozu Pb-Zn deposit, Yunnan Province, China: implications for trace-element incorporation mechanisms and ore genesis. Am. Mineral. 105, 1734–1751. https://doi.org/10.2138/am-2020-6950.

Lin, W., Wang, G., Gan, H., Wang, A., Yue, G., Long, X., Zhang, S., 2022. Heat generation and accumulation for hot dry rock resources in the igneous rock distribution areas of southeastern China. Lithosphere, 2021 (Special 5), 2039112. https://doi.org/10.2113/2022/2039112.

Liu, J., 2017. Indium mineralization in a Sn-poor skarn deposit: A case study of the Qibaoshan deposit, South China. Minerals. 7 (5), 76.

Liu, G.Q., Jin, W.Q., Zhang, L.X., Shen, K.F., 2001. Discussion on sources of metallogenetic materials of porphyry-type and hydrothermal copper deposits in northeastern Hunan Province. Geol. Mineral Resour. South China. 1, 40–47.

Liu, L.M., Peng, X.L., Wu, Y.Z., 1999. Genetic features forming vein-type gold deposits in northeastern Hunan. J. Central South Univ. Technol. 30 (01), 4–7 (in Chinese with English abstract).

Liu, H.C., Zhu, B.Q., 1994. Study on the depositional time of the Lengjiaxi Group and Banxi Group in the northwestern Hunan Province. Chin. Sci. Bull. 39 (2), 148–150 (in Chinese).

Luo, X.L., 1990. The source of ore-forming substances of Precambrian gold deposits in Hunan Province. J. Guilin Coll. Geol. 10 (01), 13–26 (in Chinese with English abstract).

Luo, K., Cugerone, A., Zhou, M.F., Zhou, J.X., Sun, G.T., Xu, J., He, K.J., Lu, M.D., 2022. Germanium enrichment in sphalerite with acicular and euhedral textures: an example from the Zhulingou carbonate-hosted Zn(-Ge) deposit, South China. Miner. Deposita 57, 1343–1365. https://doi.org/10.1007/s00126-022-01112-4.

Mao, J.W., Pirajno, F., Cook, N., 2011a. Mesozoic metallogeny in East China and corresponding geodynamic settings- an introduction to the special issue. Ore Geol. Rev. 43, 1–7.

Mao, J., Takahashi, Y., Kee, W.S., Li, Z., Ye, H., Zhao, X., Liu, K., Zhou, J., 2011b. Characteristics and geodynamic evolution of Indosinian magmatism in South China: a case study of the Guikeng pluton. Lithos 127, 535–551. https://doi.org/10.1016/j.lithos.2011.09.011.

Marty, B., Jambon, A., Sano, Y., 1989. Helium isotopes and CO_2 in volcanic gases of Japan. Chem. Geol. 76, 25–40. https://doi.org/10.1016/0009-2541(89)90125-3.

Migdisov, A.A., Zezin, D., Williams-Jones, A.E., 2011. An experimental study of Cobalt (II) complexation in Cl^- and H_2S-bearing hydrothermal solutions. Geochim. Cosmochim. Acta 75, 4065–4079.

Mizukami, M., Ohmori, S., 1989. Coprecipitation and separation of sulfide minerals in hydrothermal solutions. Mining. Geol. 39 (1), 61.

Moh, G. H., Jager, A., 1978. Phasengleichgewichte des systems Ge-Pb-Zn-S in relation zu Germanium-Gehalten alpiner Pb-Zn-Lagerstatten. Verhandlungen der Geologischen Bundesanstalt Wien, pp. 437–440.

Murakami, H., Ishihara, S., 2013. Trace elements of Indium-bearing sphalerite from tin-polymetallic deposits in Bolivia, China and Japan: A femto-second LA-ICPMS study. Ore Geol. Rev. 53, 223–243.

Nagase, T., Kojima, S., 1997. An SEM examination of the chalcopyrite disease texture and its genetic implications. Mineral. Mag. 61, 89–97. https://doi.org/10.1180/minmag.1997.061.404.09.

Ning, J.T., 2002. The native cobalt mineralization and geological condition analysis in Northeast Hunan Province, South China. Hunan Geol. 03, 192–195 (In Chinese).

Ohmoto, H., Goldhaber, M.B., 1997. Sulfur and carbon isotopes. In: Barnes, H.L. (Ed.), Geochemistry of Hydrothermal Ore Deposits, third ed. John Wiley, New York, pp. 517–611.

Ohmoto, H., Rye, R.O., 1979. Isotopes of sulfur and carbon. In: Barnes, H.L. (Ed.), Geochemistry of Hydrothermal Ore Deposits, second ed. John Wiley and Sons, New York, pp. 509–567.

Paton, C., Hellstrom, J., Paul, B., Woodhead, J., Hergt, J., 2011. Iolite: freeware for the visualisation and processing of mass spectrometric data. J. Anal. At. Spectrom 26, 2508. https://doi.org/10.1039/c1ja10172b.

Pattrick, R.A., Dorling, M., Polya, D.A., 1993. TEM study of indium-bearing and copper-bearing growth-banded sphalerite. Can. Mineral. 31, 105–117.

Pavlova, G.G., Palessky, S.V., Borisenko, A.S., Vladimirov, A.G., Seifert, T., Phan, L.A., 2015. Indium in cassiterite and ores of tin deposits. Ore Geol. Rev. 66, 99–113. https://doi.org/10.1016/j.oregeorev.2014.10. 009.

Pearce, N.J.G., Perkins, W.T., Westgate, J.A., Gorton, M.P., Jackson, S.E., Neal, C.R., Chenery, S.P., 1997. A compilation of new and published major and trace element fata for NIST SRM 610 and NIST SRM 612 glass reference materials. Geostand. Geoanalytical Res. 21, 115–144. https://doi.org/10.1111/j.1751-908X.1997.tb00538.x.

Pearson, R.G., 1963. Hard and soft acids and bases. J. Am. Chem. Soc. 85, 3533–3539. https://doi.org/10.1021/ja00905a001.

Pettke, T., Oberli, F., Audétat, A., Guillong, M., Simon, A.C., Hanley, J.J., Klemm, L.M., 2012. Recent developments in element concentration and isotope ratio analysis of individual fluid inclusions by laser ablation single and multiple collector ICP-MS. Ore Geol. Rev. 44, 10–38. https://doi.org/10.1016/j.oregeorev.2011.11.001.

Putnis, A., 2009. Mineral replacement reactions. Rev. Mineral. Geochem. 70 (1), 87–124.

Putnis, A., 2018. Mineral replacement reactions: from macroscopic observations to microscopic mechanisms. Mineral. Mag. 66, 689–708. https://doi.org/10.1180/0026461026650056.

Qiu, H.N., Wijbrans, J.R., Brouwer, F.M., Yun, J.B., Zhao, L.H., Xu, Y.G., 2010. Amphibolite facies retrograde metamorphism of the Zhujiachong eclogite, SE Dabieshan: ^{40}Ar/^{39}Ar age constraints from argon extraction using UV-laser microprobe, in vacuo crushing and stepwise heating. J. Metam. Geol. 28, 477–487.

Ramdohr, P., 1969. The ore minerals and their intergrowths. Elsevier. https://doi.org/10.1016/C2013-0-10027-X.

Reeder, R., Fagioli, R., Meyers, W., 1990. Oscillatory zoning of Mn in solution-grown calcite crystals. Earth Sci. Rev. 29, 39–46. https://doi.org/10.1016/0012-8252(0)90026-R.

Røyne, A., Jamtveit, B., Mathiesen, J., Malthe-Sørenssen, A., 2008. Controls on rock weathering rates by reaction-induced hierarchical fracturing. Earth Planet. Sci. Lett. 275 (3–4), 364–369.

Savard, D., Bouchard-Boivin, B., Barnes, S.J., Garbe-Schönberg, D., 2018. UQAC-FeS: A new series of base metal sulfide quality control reference material for LA-ICP-MS analysis. In: Proceedings of the 10th International Conference on the Analysis of Geological and Environmental Materials, Sydney, Australia, pp. 8–13.

Seifert, T., Sandmann, D., 2006. Mineralogy and geochemistry of indium-bearing polymetallic vein-type deposits: Implications for host minerals from the Freiberg district, Eastern Erzgebirge, Germany. Ore Geol. Rev. 28, 1–31. https://doi.org/10.1016/j.oregeorev.2005.04.005.

Shore, M., Fowler, A., 1996. Oscillatory zoning in minerals: A common phenomenon. Can. Mineral. 34 (6), 1111–1126.

Song, Y., Hou, Z., Xue, C., Huang, S., 2020. New mapping of the world-class Jinding Zn-Pb deposit, Lanping Basin, Southwest China: genesis of ore host rocks and records of hydrocarbon-rock interaction. Econ. Geol. 115, 981–1002. https://doi.org/10.5382/econgeo.4721.

Steiger, R.H., Jäger, E., 1977. Subcommission on geochronology: convention on the use of decay constants in geo- and cosmochronology. Earth Planet. Sci. Lett. 36, 359–362. https://doi.org/10.1016/0012-821X(77)90060-7.

Sugaki, A., Kitakaze, A., Kojima, S., 1987. Bulk compositions of intimate intergrowths of chalcopyrite and sphalerite and their genetic implications. Miner. Deposita 22, 26–32.

Wang, S.S., 1983. Age determinations of ^{40}Ar-^{40}K, ^{40}Ar-^{40}Ar and radiogenic ^{40}Ar released characteristics on K-Ar geostandards of China. Chin. J. Geol. 4, 315–323.

Wang, J.Q., Shu, L.S., Santosh, M., 2016. Petrogenesis and tectonic evolution of Lianyunshan complex, South China: insights on Neoproterozoic and late Mesozoic tectonic evolution of the central Jiangnan Orogen. Gondw. Res. 39, 114–130.

Wang, W., Wang, F., Chen, F.K., Zhu, X.Y., Xiao, P., Siebel, W., 2010. Detrital zircon ages and Hf-Nd isotopic composition of Neoproterozoic sedimentary rocks in the Yangtze Block: constraints on the deposition age and provenance. J. Geol. 118 (1), 79–94.

Wang, Z., Xu, D., Chi, G., Shao, Y., Lai, J., Deng, T., Guo, F., Wang, Z., Dong, G., Ning, J., Zou, S., 2017. Mineralogical and isotopic constraints on the genesis of the Jingchong Co–Cu polymetallic ore deposit in northeastern Hunan Province, South China. Ore Geol. Rev. 88, 638–654. https://doi.org/10.1016/j.oregeorev.2017.02.011.

Wang, Z., Wang, Y., Peng, E., Zou, S., Deng, T., Lai, F., Ning, J., Dong, G., Xu, D., 2022. Micro-textural and chemical fingerprints of hydrothermal cobalt enrichment in the Jingchong Co-Cu polymetallic deposit, South China. Ore Geol. Rev. 142 https://doi.org/10.1016/j.oregeorev.2022.104721.

Wang, X.L., Zhou, J.C., Griffin, W.L., Wang, R.C., Qiu, J.S., O'reilly, S.Y., Xu, X.S., Liu, X.M., Zhang, G.L., 2007. Detrital zircon geochronology of Precambrian basement sequences in the Jiangnan orogeny: dating the assembly of the Yangtze and Cathaysia Blocks. Precambr. Res. 159 (1), 117–131.

Wang, X.L., Ma, C.Q., Zhang, C., Zhang, J.Y., Marks, M.A., 2014b. Genesis of leucogranite by prolonged fractional crystallization: a case study of the Mufushan complex, South China. Lithos 206, 147–163.

Wang, W., Zhou, M.F., Yan, D.P., Li, J.W., 2012. Depositional age, provenance, and tectonic setting of the Neoproterozoic Sibao Group, southeastern Yangtze Block, South China. Precambr. Res. 192, 107–124.

Wang, W., Zhou, M.F., Yan, D.P., Li, L., Malpas, J., 2013. Detrital zircon record of Neoproterozoic active-margin sedimentation in the eastern Jiangnan Orogen, South China. Precambr. Res. 235, 1–19.

Wang, X.L., Zhou, J.C., Griffin, W.L., Zhao, G., Yu, J.H., Qiu, J.S., Zhang, Y.J., Xing, G.F., 2014a. Geochemical zonation across a Neoproterozoic orogenic belt: isotopic evidence from granitoids and metasedimentary rocks of the Jiangnan orogeny, China. Precambr. Res. 242, 154–171.

Watson, E.B., Liang, Y., 1995. A simple model for sector zoning in slowly grown crystals: Implications for growth rate and lattice diffusion, with emphasis on accessory minerals in crustal rocks. Am. Mineral. 80 (11–12), 1179–1187.

Wiggins, L.B., Craig, J.R., 1980. Reconnaissance of the Cu-Fe-Zn-S system; sphalerite phase relationships. Econ. Geol. 75, 742–751. https://doi.org/10.2113/gsecongeo.75.5.742.

Wilson, S.A., Ridley, W.I., Koenig, A.E., 2002. Development of sulfide calibration standards for the laser ablation inductively-coupled plasma mass spectrometry technique. J. Anal. Spectrom. 17, 406–409. https://doi.org/10.1039/B108787H.

Wilson, S.A., 2019. G-probe 21 summary report. International Association of Geoanalysts, pp. 1–14. http://www.geoanalyst.org/wp- content/uploads/2021/02/GP-21-report.pdf.

Xu, J., Cook, N.J., Ciobanu, C.L., Li, X., Kontonikas-Charos, A., Gilbert, S., Lv, Y., 2020. Indium distribution in sphalerite from sulfide-oxide-silicate skarn assemblages: a case study of the Dulong Zn-Sn-In deposit, Southwest China. Miner. Deposita 56, 307–324. https://doi.org/10.1007/s00126-020-00972-y.

Xu, D., Deng, T., Chi, G., Wang, Z., Zou, F., Zhang, J., Zou, S., 2017. Gold mineralization in the Jiangnan Orogenic Belt of South China: geological, geochemical and geochronological characteristics, ore deposit-type and geodynamic setting. Ore Geol. Rev. 88, 565–618.

Xu, D.R., Wang, L., Li, P.C., Chen, G.H., He, Z.L., Fu, G.G., Wu, J., 2009. Petrogenesis of the Lianyunshan granites in northeastern Hunan Province, South China, and its geodynamic implications. Acta Petrol. Sin. 25, 1056–1078 (in Chinese with English abstract).

Xu, D., Yu, D., Wang, Z., Li, B., Chi, G., Zhou, Y., Zou, S., Deng, T., Zhang, S., Wang, X., 2022. Zircon U-Pb and muscovite 40Ar/39Ar dating of Pb-Zn-(Cu) polymetallic deposits in northeastern Hunan Province, Jiangnan Orogen: Evidence for large-scale mineralization in South China at ca. 150–120 Ma. Ore Geol. Rev. 150, 105200 https://doi.org/10.1016/j.oregeorev.2022.105200.

Yao, J.L., Shu, L.S., Santosh, M., Zhao, G.C., 2014. Neoproterozoic arc-related mafic–ultramafic rocks and syn-collision granite from the western segment of the Jiangnan Orogen, South China: constraints on the Neoproterozoic assembly of the Yangtze and Cathaysia Blocks. Precambr. Res. 243, 39–62.

Ye, L., Cook, N.J., Ciobanu, C.L., Yuping, L., Qian, Z., Tiegeng, L., Wei, G., Yulong, Y., Danyushevskiy, L., 2011. Trace and minor elements in sphalerite from base metal deposits in South China: a LA-ICPMS study. Ore Geol. Rev. 39, 188–217. https://doi.org/10.1016/j.oregeorev.2011.03.001.

Yi, Z.S., Luo, X.Y., Zhou, D.H., Xiao, C.Y., 2010. Geological characteristics and genesis of Jinchong Co-Cu polymetal Deposit, Liuyan, Hunan Province. Geol. Miner. Resour. South China 03, 12–18 (in Chinese with English abstract).

Yu, D., Xu, D., Zhao, Z., Huang, Q., Wang, Z., Deng, T., Zou, S., 2020. Genesis of the Taolin Pb-Zn deposit in northeastern Hunan Province, South China: constraints from trace elements and oxygen-sulfur-lead isotopes of the hydrothermal minerals. Miner. Deposita 55, 1467–1488. https://doi.org/10.1007/s00126-019-00947-8.

Yu, D., Xu, D., Wang, Z., Xu, K., Huang, Q., Zou, S., Zhao, Z., Deng, T., 2021. Trace element geochemistry and O-S-Pb-He-Ar isotopic systematics of the Lishan Pb-Zn-Cu hydrothermal deposit, NE Hunan, South China. Ore Geol. Rev. 133 https://doi.org/10.1016/j.oregeorev.2021.104091.

Yuan, S., Mao, J., Zhao, P., Yuan, Y., 2018. Geochronology and petrogenesis of the Qibaoshan Cu-polymetallic deposit, northeastern Hunan Province: implications for the metal source and metallogenic evolution of the intracontinental Qinhang Cu-polymetallic belt, South China. Lithos 302, 519–534.

Zhang, J., Liu, H.B., Li, J.J., Jin, G.S., Han, J., Zhang, J.F., 2014. Advances in the study of ^{40}Ar-^{39}Ar isotopic dating method. World Nucl. Geosci. 31 (1), 53–58.

Zhao, G.C., 2015. Jiangnan Orogen in South China: developing from divergent double subduction. Gondw. Res. 27 (3), 1173–1180.

Zhao, J., Brugger, J., Xia, F., Ngothai, Y., Chen, G., Pring, A., 2013. Dissolution-reprecipitation vs. solid-state diffusion: Mechanism of mineral transformations in sylvanite, (AuAg) $_2$Te$_4$, under hydrothermal conditions. Am. Mineral. 98 (1), 19–32.

Zhao, G., Cawood, P.A., 2012. Precambrian geology of China. Precambr. Res. 222, 13–54.

Zhao, J.S., Qiu, X.L., Zhao, B., Tu, X.L., Yu, J., Lu, T.S., 2007. REE geochemistry of mineralized skarns from Daye to Wushan region, China. Geochim 36 (4), 400–412 (in Chinese with English abstract).

Zhao, H., Shao, Y., Zhang, Y., Cao, G., Zhao, L., Zheng, X., 2023. Big data mining on trace element geochemistry of sphalerite. J. Geochem. Explor. 107254. https://doi.org/10.1016/j.gexplo.2023.107254.

Zhong, R., Brugger, J., Chen, Y., Li, W., 2015. Contrasting regimes of Cu, Zn and Pb transport in ore-forming hydrothermal fluids. Chem. Geol. 395, 154–164. https://doi.org/10.1016/j.chemgeo.2014.12.008.

Zhou, J.X., Wang, X.C., Wilde, S.A., Luo, K., Huang, Z.L., Wu, T., Jin, Z.G., 2018. New insights into the metallogeny of MVT Zn-Pb deposits: A case study from the Nayongzhi in South China, using field data, fluid compositions, and in situ S-Pb isotopes. Am. Mineral. 103, 91–108. https://doi.org/10.2138/am-2018-6238.

Zhou, Y., Xu, D., Dong, G., Chi, G., Deng, T., Cai, J., Ning, J., Wang, Z., 2021. The role of structural reactivation for gold mineralization in northeastern Hunan Province, South China. J. Struct. Geol. 145 https://doi.org/10.1016/j.jsg.2021.104306.

Zhou, M.F., Yan, D.P., Kennedy, A.K., Li, Y., Ding, J., 2002a. SHRIMP U-Pb zircon geochronological and geochemical evidence for Neoproterozoic arc-magmatism along the western margin of the Yangtze Block, South China. Earth Planet. Sci. Lett. 196, 51–67.

Zhou, M.F., Kennedy, A.K., Sun, M., Malpas, J., Lesher, C.M., 2002b. Neoproterozoic arcrelated mafic intrusions along the northern margin of South China: implications for the accretion of Rodinia. J. Geol. 110, 611–618.

Zhu, Z.Y., Jiang, S.Y., Ciobanu, C.L., Yang, T., Cook, N.J., 2017. Sulfur isotope fractionation in pyrite during laser ablation: Implications for laser ablation multiple-collector inductively coupled plasma mass spectrometry mapping. Chem. Geol. 450, 223–234. https://doi.org/10.1016/j.chemgeo.2016.12.037.

Zhu, K.Y., Jiang, S.Y., Su, H.M., Duan, Z.P., 2021. In situ geochemical analysis of multiple generations of sphalerite from the Weilasituo Sn-Li-Rb-Cu-Zn ore field (Inner Mongolia, northeastern China): implication for critical metal enrichment and ore-forming process. Ore Geol. Rev. 139 https://doi.org/10.1016/j.oregeorev.2021.104473.

Zhuang, L., Song, Y., Liu, Y., Fard, M., Hou, Z., 2019. Major and trace elements and sulfur isotopes in two stages of sphalerite from the world-class Angouran Zn-Pb deposit, Iran: implications for mineralization conditions and type. Ore Geol. Rev. 109, 184–200. https://doi.org/10.1016/j.oregeorev.2019.04.009.

Zou, S., Zou, F., Ning, J., Deng, T., Yu, D., Ye, T., Xu, D., Wang, Z., 2018. A stand-alone Co mineral deposit in northeastern Hunan Province, South China: its timing, origin of ore fluids and metal Co, and geodynamic setting. Ore Geol. Rev. 92, 42–60. https://doi.org/10.1016/j.oregeorev.2017.11.008.